RESEARCH ARTICLE

Short-term biogeomorphology of a gravel-bed river: Integrating remote sensing with hydraulic modelling and field analysis

Melissa Latella[1,2] | Davide Notti[3] | Marco Baldo[3] | Daniele Giordan[3] | Carlo Camporeale[1]

[1]Department of Environment, Land and Infrastructure Engineering (DIATI), Politecnico di Torino, Torino, Italy

[2]Impacts on Agriculture, Forests and Ecosystem Services (IAFES) Division, Fondazione Centro Euro-Mediterraneo sui Cambiamenti Climatici (CMCC), Viterbo, Italy

[3]Research Institute for Geo-hydrological Protection (CNR-IRPI), National Research Council, Torino, Italy

Correspondence
Melissa Latella and Carlo Camporeale, Department of Environment, Land and Infrastructure Engineering (DIATI), Politecnico di Torino, 10129 Torino, Italy.
Email: melissa.latella@cmcc.it and carlo.camporeale@polito.it

Abstract

In recent decades, fluvial geomorphology and ecohydraulic research have extensively used field observations, remote sensing or hydrodynamic modelling to understand river systems. This study presents an innovative approach that combines field surveys, Light Detection and Ranging (LiDAR)-based topographical and biomass analyses and model-derived hydro-morphodynamic geostatistics to examine short-term biogeomorphological changes in the wandering gravel-bed Orco River in Italy. Our primary hypothesis is that hydro-morphological variables can be robust descriptors for riparian vegetation distribution. From a geomorphological perspective, our study confirms the prevalent wandering behaviour of the Orco River. Moreover, we identified a widening trend in braiding and anabranching sections, particularly downstream. This is evident because of hotspots of flood-induced morphological reactivation and the redistribution of sediments from the riverbed to lateral bars, resulting in a multi-thread pattern. Our analysis reveals a net increase in biomass during the observation period despite frequent flood disturbances. We attributed it to two opposing biogeomorphological dynamics: the reduced flow disturbance in some regions due to flood-induced geomorphological changes and the self-healing of lateral connectivity through river wandering. Such a net increase indicates that transitional rivers store carbon in the form of vegetation biomass due to their short-term morphological instability and the different timescales between vegetation and morphological adjustments. Finally, we supported our initial hypothesis with three key findings: (i) a signature of vegetation not just on topography but also on hydro-morphological conditions, summarised by inundation probability; (ii) the lower variance in vertical topographical changes in vegetated areas compared with bare ones; and (iii) the introduction of a new parameter, named *inundation viscosity*, derived from the product of mean bed shear stress and average inundation duration, as a discriminating factor for colonisation conditions. These results underscore the value of our comprehensive approach.

KEYWORDS
biogeomorphology, ecomorphodynamics, field measurements, fluvial landforms, hydrodynamic modelling, LiDAR, riparian vegetation

1156 | wileyonlinelibrary.com/journal/esp

Earth Surf. Process. Landforms. 2024;49:1156–1178.

1 | INTRODUCTION

Throughout history, rivers experienced different anthropogenic disturbances that impacted their sediment budget and water-sediment connectivity between the active channels and the surrounding floodplain more than expected from their natural channel evolution (Best, 2019; Maaß et al., 2021; Messerli et al., 2000; Notebaert & Verstraeten, 2010; Rinaldi, 2003; Surian & Rinaldi, 2003; Surian, Rinaldi, et al., 2009, Surian, Ziliani, et al. 2009; Vanmaercke et al., 2015). Most of the human footprint on watercourses is linked to direct alterations, such as river training, damming and sediment mining, that attempt to answer to the continuous demand for lands to crop, water storage and supply, flood protection, energy and construction materials (Comiti et al., 2011; Downs & Piégay, 2019; Nilsson et al., 2005; Wohl, 2018). Moreover, rivers respond to off-site alterations related to urban sprawl, socio-economical forcing and land use, like afforestation and deforestation practices, that can influence their sediment budgets and spatio-temporal evolution (Gregory, 2006; Kayitesi et al., 2022; Maaß et al., 2021; Wohl, 2018; Scorpio & Piégay, 2021).

After decades of significant human-induced disruption, the trajectories of certain gravel-bed European rivers began to shift in the 1970s (Brown et al., 2018; Surian, Rinaldi, et al., 2009; Surian, Ziliani, et al., 2009). This shift was partly a result of policies regulating mining activities in river corridors, aiming to balance sediment starvation. However, it is also linked to the increased incidence of major floods induced by climate change, causing numerous river systems to respond with unexpected reactivation of secondary channels, changes in floodplain morphology and an overall rise in connectivity (Karim et al., 2015; Maaß et al., 2021; Martínez-Fernández et al., 2018; O'Briain, 2019). In some rivers, even the presence of dams cannot entirely prevent this response, as hydropeaking affects regular flows but inadequately mitigates extreme floods (Nigrelli & Audisio, 2010). Consequently, due to frequent major floods, many rivers tend to revert to their original braided form, assuming a transitional (i.e., wandering) behaviour that is challenging to predict. This behaviour can complicate sediment management and restoration planning (Rinaldi, 2003).

Fluvial wandering might favour lateral connectivity and the health of riparian ecosystems, including vegetation. Several works have highlighted the role of vegetation on rivers' trajectories (Bendix & Stella, 2022; Corenblit et al., 2007; Gurnell, 2014; Hupp & Osterkamp, 1996; Osterkamp et al., 2012). For example, the soil–root interaction is well recognised to increase cohesion (Edmaier et al., 2011), while above-ground biomass influences sediment transport, deposition patterns, channel migration and chute cutoff occurrence (Constantine et al., 2010; Dufour et al., 2015; Gurnell & Grabowski, 2016; Liébault & Piégay, 2002; Scorpio & Piégay, 2021). Furthermore, some works have remarked on the linkage of riverine and riparian trajectories with meteo-hydrological conditions and anthropogenic pressure across fluvial systems (Garófano-Gómez et al., 2017; Latella et al., 2020; Liébault & Piégay, 2002). However, the literature on gravel-bed rivers has generally disregarded the overall nexus among climate, anthropogenic factors, hydrodynamics and vegetation in the floodplain (Dawson et al., 2022; Downs & Piégay, 2019; Langat et al., 2019; Liébault & Piégay, 2002; Rumsby & Macklin, 1994; Surian & Rinaldi, 2003; Surian, Rinaldi, et al., 2009; Surian, Ziliani, et al., 2009; Turitto et al., 2010), just focusing on some

particular aspect of this interaction (e.g., the stabilising role of plants after channel narrowing; see Rinaldi, 2003).

The present work aims to adopt an innovative combination of multi-temporal data and methods to unveil the interaction among hydrodynamics, riparian vegetation and sediment dynamics (i.e., the biogeomorphological triad, sensu D'Alpaos et al., 2016), specifically focusing on the short-term dynamics of a transitional (wandering) vegetated fluvial corridor. We applied such a combination of data and methods to the Orco River in north-west Italy and its floodplain during both ordinary flow regimes and three exceptional floods with the purpose of exploring the biogeomorphological response to flood disturbance and some short-term processes like plant colonisation.

The novelty of this investigation is the application of an *integrated approach* that combines various tools traditionally implemented individually. Specifically, these tools encompass field surveys, Light Detection and Ranging (LiDAR)-based topographical and biomass analyses and model-derived hydro-morphological geostatistical parameters. This integration offers a new viewpoint on fluvial processes and addresses the need for multidisciplinary efforts to advance biogeomorphological research (Molau, 2008; Rodríguez-González et al., 2022; Viles, 2020). Indeed, it is worth noticing that, although fluvial biogeomorphology has recently seen a bloom of advanced techniques to study natural and anthropogenic processes from stereophotogrammetric data, multispectral or hyperspectral imagery (e.g., Demarchi et al., 2017; Godfroy et al., 2023; Roux et al., 2015; Salerno et al., 2022; Vautier et al., 2016), a complementary integration with hydraulic modelling and geostatistics is still lacking.

A similar approach was initially introduced by Latella et al. (2020), where the calibration of a minimalist ecohydrological riparian model was employed using real data to explore the potential of hydro-morphological statistics in characterising the dynamics of riparian vegetation biomass. However, this study was confined to a very limited geographical area, comprising only two fluvial bars, and did not consider temporal variations. Consequently, it called for further research to substantiate its theoretical findings. In contrast, the present work extends and diverges from the approach in Latella et al. (2020). Rather than focusing on model calibration, we here prioritise gaining a deeper understanding of riparian processes. Moreover, we expand our investigation to encompass both broader temporal and spatial scales because the work spans a 2-year observation period across a 30 km stretch of a wandering river. Specifically, our overarching objective is to assess the utility of model- and data-based hydro-morphological descriptors within the realm of fluvial biogeomorphology in order to unveil new statistical features of the mutual interactions among hydrodynamics, morphodynamics and riparian vegetation dynamics. We will show that this approach can unveil unanticipated facets of the biogeomorphological processes.

The paper is outlined as follows: Section 2 describes the study site, an overview of data collection and processing with the adopted integrated methodology; Section 3 reports the results derived from centreline analysis, morphological change detection and biomass budgeting by comparing 2021 with 2019 scenarios and emphasising differences among the investigated reaches; Section 5 discusses the evidence of the biogeomorphological feedback through a cross-analysis of the obtained data from a broader perspective by commenting on the observed key processes; finally, Section 5 draws general insights about gravel-bed wandering rivers.

2 | MATERIALS AND METHODS

2.1 | Study site

The Orco River, located in north-west Italy (45°14′45.97″N–7°48′29.67″E), is approximately 85 km long and has a catchment area of 930 km². It is bounded downstream by its confluence with the Po River (Figure 1a). Our study focuses on a 34 km segment, extending from Cuorgné to Chivasso, corresponding to the plain-alluvial part of the basin. This segment exhibits erosion–deposition phenomena typical of wandering/pseudo-meandering river planforms (Nigrelli & Audisio, 2010).

Several previous studies have investigated the Orco River, identifying two distinct segments with varying geomorphological and sedimentation processes (Bizzi et al., 2019; Demarchi et al., 2017; Lollino et al., 2005; Pellegrini et al., 2008; Turitto et al., 2010). From Courgné to Rivarolo (Figure 1b,c), the river features a mean slope of 0.9% to 1%, pebbly deposits with a gravel matrix and a single-thread channel with a tendency to bed lowering. Along this stretch, remnants of an ancient conoid propagating down towards the plain, nearly reaching Rivarolo, can be observed. Downstream of Rivarolo, up to its confluence with the Po River, the Orco River exhibits a milder slope (0.5%

to 0.3%) and multi-thread/wandering morphology, with prevalent gravel deposits within a sandy matrix. The median grain size (d_{50}) for this reach is 7.5 cm.

The evolution of the Orco River has followed the trajectories of other gravel-bed streams in Italy, as described by the concerning literature (see Surian & Rinaldi, 2003; Surian, Rinaldi, et al., 2009, for a review). Historical maps testify that the Orco River was braided until the late nineteenth century. In the early twentieth century, urban migration from the mountains and land use changes, including the replacement of pastures with forests, reduced sediment supply from hillslopes to the river (Surian, Rinaldi, et al., 2009). In addition, the construction of levees and bank protection structures, damming (a system of six artificial reservoirs for hydroelectric supply was built between the 1930s and 1950s) and mining contributed to river degradation, resulting in channel narrowing and severe bed degradation. The downstream part of the Orco catchment experienced significant bed lowering, with an average decrease of approximately 1.0–2.0 m and a local maximum of 3.5 m (Turitto et al.2008; Turitto et al., 2010). Thus, the Orco River transformed from a braided system into a single-thread river (Pellegrini et al., 2008; Surian, Rinaldi, et al. 2009; Turitto et al., 2008, 2010). The cessation of mining activities in the 1980s, coupled with the occurrence of exceptional floods since the 2000s, has

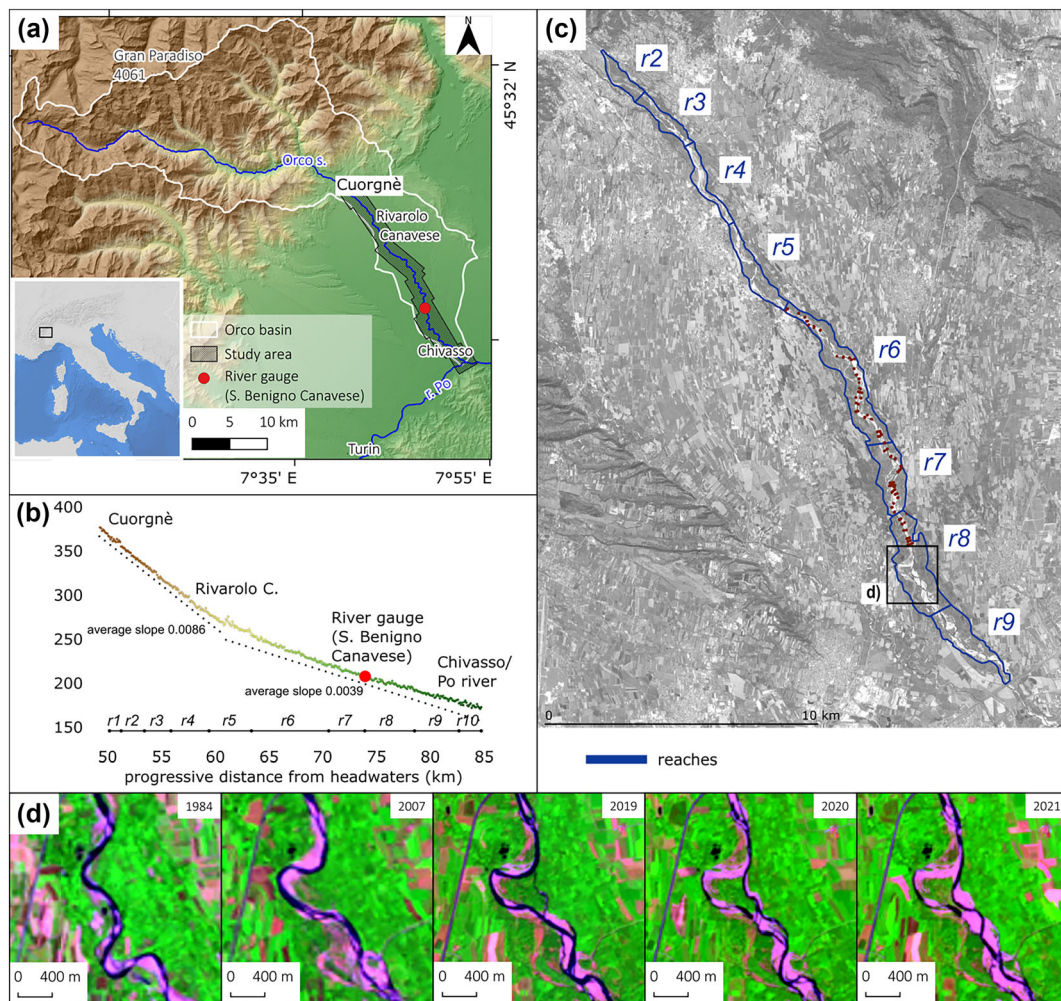**FIGURE 1** (a) Location of the study site, the lower part of the Orco River in north-west Italy. (b) Elevation profile of the segment. (c) Visualisation of the chosen reaches (blue) and location of the measured cross-sections (red). (d) Time evolution (1984–2021) of a meander within the study site from Landsat4-5,8 and Sentinel-2 satellite images. [Color figure can be viewed at wileyonlinelibrary.com]

partially reversed the narrowing process (Pellegrini et al., 2008; Surian, Rinaldi, et al. 2009). Over the 20th century, channel width reduced by 68% in the lowest section of the catchment, while widened up to 39% from 1975 to 2003 (both percentages are relative to the width at the end of the 18th century, as reported by Surian, Rinaldi, et al. (2009).

At present, the Orco River is a *transitional* (or transient) river, both in terms of its geomorphology (Rinaldi et al., 2012) and spatio-temporal behaviour. While experiencing continuous bed degradation and channel simplification during ordinary regimes, it responds actively to exceptional floods with moderate lateral migration of meanders and significant morphological modifications, particularly in its downstream section (e.g., Figure 1d). Such behaviour has been documented during the 1994 and 2000 floods, which had a return time equal to or greater than 20 years (Cassardo et al., 2006; Pellegrini et al., 2008). The local impact of this kind of events depends on biogeomorphological processes. For instance, field observations have shown reduced erosion in vegetated areas, while certain local geological conditions (e.g., Pleistocene lacustrine sand deposits) facilitate lateral migration.

Human activities poorly impaired the ecological functionality of the Orco River's aquatic ecosystem and its riparian corridor (ARPA, 2021). Submerged vegetation is relatively rare, except for herbaceous species colonising sand deposits, and is not considered in this work. Riparian vegetation consists of juvenile individuals of poplars (*Populus tremula* L., *Populus alba* L. and *Populus nigra* L.) and willows (*Salix alba* L. and *Salix purpurea* L.) on the river bars. The floodplain hosts more mature willows and poplars along with adult black locusts (*Robinia pseudoacacia* L.), European oaks (*Quercus robur* L.) and hornbeams (*Carpinus betulus* L.).

As explained in Section 2.4, our work focuses on the area subjected to a 20-year return time flood, which represents the most exceptional event during our observation period. We made slight modifications to remove crops or houses, resulting in a total area of interest (AoI) of approximately 16 km^2. To facilitate our analysis, we divided the AoI longitudinally into 10 reaches based on hydro-geomorphological evidence, such as flow direction and the lateral extent of flooded areas. In the following, we label each reach as r1 to r10 (Figure 1c). However, we only considered results related to r2–r9, excluding r1 and r10 due to numerous interferences with structures, such as highway bridges or hydropower dams, which could potentially undermine the integrity of our analysis.

The chosen study site offers an excellent opportunity for short-term monitoring because the Orco River's morphology undergoes abrupt changes in response to flood pulses. Finally, due to its propensity for landform reworking, lateral migration and vegetation uprooting, the Orco River has become the main focus of regional monitoring and restoration programmes (e.g., the first general programme of sediment management for Piedmont's watercourses Rosso et al., 2008). These programmes highlight the challenges associated with managing transitional gravel-bed rivers.

2.2 | Field surveys

As reported in Latella et al. (2021) and Latella et al. (2022), we carried out extensive field surveys at the study site between February 2019 and May 2021 (Figure 1). All the surveys encompassed three different activities.

First, we sampled sediment using the *Wolman Pebble Count* technique for the coarser sediment fractions. The Wolman Pebble count consists of the random collection of samples following a zigzag path and the subsequent measurement of their intermediate axis (Wolman, 1954). The finer classes (<2 mm) were analysed through sieving. We found a d_{50} of approximately 0.075 m and a d_{90} of 0.170 m.

Second, we measured the bathymetry across 41 river cross-sections in reaches r6–r8 (Figure 1c). The low-flow conditions met during the campaign allowed us to manually measure the bed position with a Global Positioning System (GPS) sensor in real-time kinematic (RTK) mode, achieving centimetric accuracy. In the few areas where water depth impeded our ability to ford the river, we utilised a water current profiler (SonTek ADP—Acoustic Doppler Profiler) mounted on a small boat. When combined with a GPS antenna, this system delivered bathymetry data with a precision of approximately 0.025 m.

Third, we measured the main geometrical features of mature vegetation (tree height and the diameter at breast height) and shrubs (volume, geometry and biomass). The Supporting Information provides further details about these measurements.

In addition to field measurements, two airborne laser scanner (ALS) acquisitions were carried out on 28th February 2019 and 23rd March 2021 by the Italian National Research Council—Research Institute for Geo-Hydrological Protection (CNR-IRPI) with a resolution of 9 points·m^{-2} and vertical accuracy equal to 0.1 m. RGB orthophotos were provided alongside the ALS data with a pixel resolution of 0.07 m. These ALS surveys were planned in a period of minimal stream discharge (3 and 10 m^3·s^{-1} in 2019 and 2021, respectively) and reduced vegetation activity (i.e., plant-dormant phase).

2.3 | Hydrology

The Regional Agency for the Protection of the Environment (ARPA-Piemonte) provided daily flow rate data from the gauging station located at San Benigno Canavese (45°14′48.72″–7°48′23.10″E, Figure 1a), whose first measurement dates back to 1st January 2002. Data reveal a sub-alpine hydrological behaviour. Throughout the year, a first flow rate peaks occur in late spring or early summer because of snowmelt, while a second group of peaks results from intense floods caused by autumn rainfalls. Dry periods usually occur in late summer and winter (Figure 2). The annual mean daily flow rate is 21.0 m^3·s^{-1}. Mean return time flow rates are 422, 670, 1300, 2020, 2370 and 2870 m^3·s^{-1} corresponding to return periods of 2, 5, 20, 100, 200 and 500 years, respectively (Camporeale et al., 2021; Rosso et al., 2008).

Three major floods occurred during our observation period: two 2-year return time floods on 24 October 2019 (ARPA, 2019a) and 24 November 2019 (ARPA, 2019b) and one 20-year return time flood on 3 October 2020, commonly named *Alex storm* (ARPA, 2020). The 2019 discharge peaks caused a severe meander cutoff and several morphological changes successively enhanced by the Alex storm. We notice that the upstream dams poorly dampen major floods, which are the hydrological driver of river evolution (Nigrelli & Audisio, 2010; Surian & Rinaldi, 2003), although they contribute to the downstream sediment starvation.
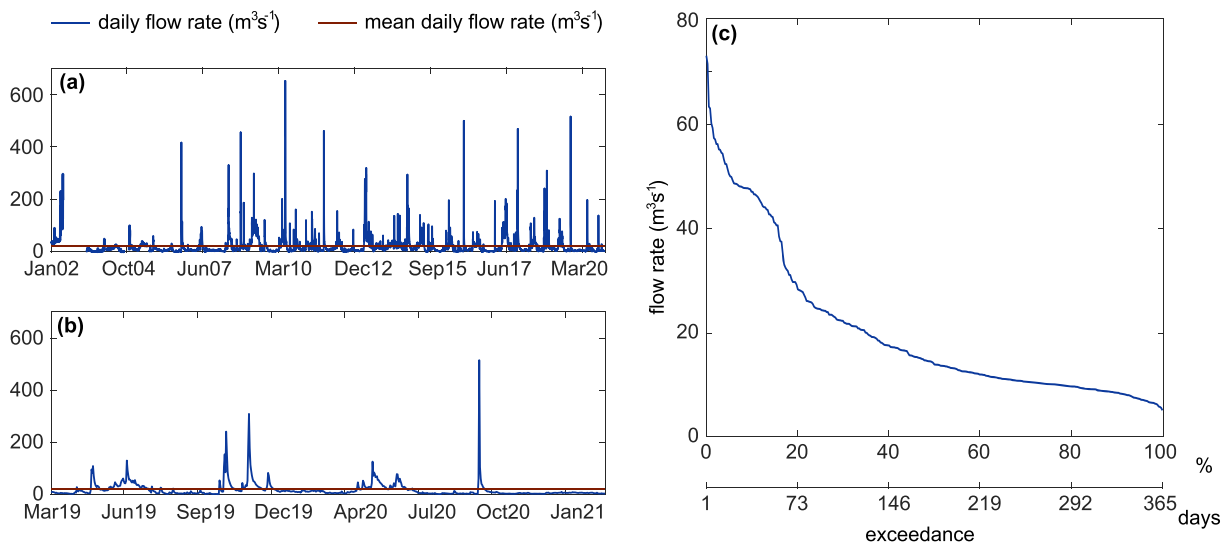
FIGURE 2 Flow rate time series of (a) the available years and (b) the observation period at the San Benigno Canavese gauging station. Blue lines indicate the daily time series, whereas red lines indicate the average value. (c) Duration curve of the average annual time series. [Color figure can be viewed at wileyonlinelibrary.com]

2.4 | Topographical and bathymetric reconstruction

After each ALS survey, we followed the procedure outlined by Baldo et al. (2009) to process the raw LiDAR point cloud data. We used the TERRASOLID package within the MICROSTATION environment for trajectory adjustment, boresight calibration and orthomosaic production. Subsequently, the LiDAR dataset underwent filtering and classification through geometric and echo-based macroclassification routines. This process allowed us to obtain an initial ground surface (i.e., a digital terrain model [DTM]) and a secondary overground class. After validating the first DTM ground class, we used a height-based algorithm to extract a secondary vegetation class, categorised into low, medium and high vegetation. The points excluded from the vegetation cloud were assigned to the final ground class to enhance the DTM's resolution. Because the reliability of the generated DTM was crucial for the forthcoming analysis, we validated it on the basis of more than 90 ground control points (GCPs) georeferenced during a global navigation satellite system-real-time kinematic (GNSS-RTK) campaign. Finally, we reduced the DTM to a geodetic model using the Italian ITALGEO 2005 geoid and utilised AGISOFT METASHAPE and Cloud Compare software to generate the final DTMs and the accompanying orthophotos. The final DTM resolution was 0.1 m, later downsampled to a grid of 16 million of 1×1 m cells for the biomass and geomorphic analyses, as described in Sections 2.7, 2.8. Additionally, a grid of 640,000 cells measuring 5×5 m was used for hydrodynamic simulations, as illustrated in Section 2.5.

The LiDAR sensors used during the ALS acquisitions (LiteMapper 6800) have a wavelength that does not allow for water penetration. Although river discharge was minimal during the two LiDAR surveys, it was necessary to infer the bathymetry of the wet channel during acquisition. For this purpose, we followed a *rectangularisation* procedure, which enabled us to define rectangular cross-sections with geometric and physical features that ensure hydraulic equivalence with the actual channel configuration (see, e.g., Peña & Nardi, 2018). Further details can be found in the Supporting Information.

We validated the rectangularisation procedure by comparing the direct in-field measurements taken in 2019 and the average channel depths computed through the bathymetric correction (Figure 3) at each cross-section. The average depth error between the measured and the corrected cross-sections is -0.45 m. Consequently, the procedure resulted in an overall overestimation of water depth, which is likely attributed to the underestimation of channel width during the LiDAR data analysis. Considering the average features of the area where the cross-sections were measured (discharge $Q = 10.17$ m·s^{-1}; slope $S = 0.0042$; Manning coefficient $n = 0.03$ s·m$^{-1/3}$) and after applying the Chezy law, it emerges that the average width underestimation is 5.6 m. This error is reasonable because the LiDAR sensor used may provide the bathymetry beneath very shallow water or return the water surface under specific lighting conditions.

2.5 | Hydrodynamic modelling

We carried out hydrodynamic modelling as a first step to calculate the space-time features of the hydraulic factors influencing hydromorphological changes, specifically focusing on water depths, velocities and bed shear stress. The model output allowed us to delineate the AoI according to the 20-year return time flood map (corresponding to about 16 km^2). Also, it enabled us to compute some spatially distributed hydrodynamic statistics, such as the inundation probability and the time memory of the inundation process, that we later compared with biogeomorphological changes (see details in Section 2.7).

To achieve this, we performed a two-dimensional depth-averaged hydrodynamic modelling using the shallow-water numerical solver *Delft3D*. The model employed a square-cell grid with 5 m resolution, which was interpolated over the generated DTM and the reconstructed bathymetry. We set the upstream and downstream boundary conditions as arbitrary flow rates and a Riemann invariant equal to zero to prevent wave reflection, respectively. In total, we performed 25 simulations (Tables 1 and 2).
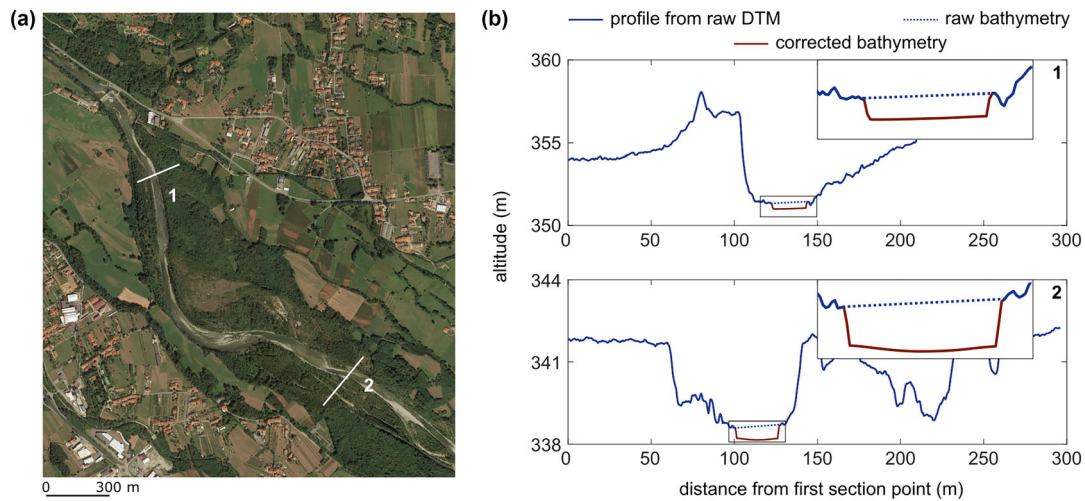
FIGURE 3 (a,b) Example of bathymetry correction of two cross-sections in r2. Blue lines indicate the profile deriving from raw LiDAR data (notice the gap due to LiDAR signal absorption by water). Red lines indicate the reconstructed rectangular channel. [Color figure can be viewed at wileyonlinelibrary.com]

TABLE 1 Parameter setting of Delft3D software for hydrodynamic modelling.

Parameter	Value	Unit	Notes
Maximum Courant number	0.7	-	Based on software guidelines
Modelled area (width × length)	Approximately 1 200 × 26 000	m	-
Square-cell size (width × height)	5 × 5	m	Resolution–efficiency compromise
D_{50}	0.07	m	From collected field data
Manning coefficient of the bare ground (s·m$^{-1/3}$)	0.033	-	From collected field data
ID of *trachytope* formula for bare areas	53	-	Manning coefficient
ID of *trachytope* formula for vegetated areas	154	-	Formula (Baptist et al., 2007)

The first set of simulations assumed bare soil and utilised Strickler–Manning's law to define the bed roughness. Subsequently, we repeated the simulations including the values of Chezy's coefficient for each computational cell based on the results of the previous bare-soil simulations. This step also involved accounting for flow resistance due to emerged vegetation, for which we adopted the formulation by Baptist et al. (2007) and provided the required vegetation geometry and the stem density by processing the LiDAR point cloud (Section 2.8). We set the other parameters related to vegetation resistance in agreement with the literature (e.g., Oorschot et al.2016).

The software gave the two-dimensional flow field and the water level distribution across the whole domain as output. We initially validated these results by comparing the average water level near the San Benigno gauging station with the measured values for a set of representative flow rates (Table 2). The error between the modelled and the measured water levels is 0.096 m, which is reasonably acceptable because it falls below the overall accuracy of the corrected DTM. DTM accuracy was computed by considering two independent sources of uncertainty in the DTM generation: (i) the vertical accuracy of the LiDAR sensors ($\sigma_{LiDAR} = 0.1$ m) and (ii) the noise generated in the LiDAR point cloud by the coarse grain size ($\sigma_{grain} = 0.075$ m). The overall accuracy resulted in $\sigma_{DTM} = \sqrt{\sigma_{LiDAR}^2 + \sigma_{grain}^2} = 0.125$ m.

We conducted a second, qualitative, validation across the entire AoI involving the visual inspection of the modelled flood maps and their comparison with cloud-free satellite images provided by Sentinel-2 (see the Supporting Information).

We post-processed the results by fitting a power-law rating curve between water levels h and flow rates Q for each computational cell. By applying these rating curves to the available 20-year flow rate time series, we obtained water level time series $h_k(t)$ for each kth computational cell and the corresponding probability density function of water levels $p_k(h)$. This information allowed us to define three crucial statistical descriptors of local hydrometry,

$$P_I = \int_{\eta(x,y)}^{\infty} p(h)dh, \quad \tau = \left(\frac{1}{T_i} + \frac{1}{T_e}\right)^{-1}, \quad \mathcal{I} = \frac{T_i}{T_e} = \frac{P_I}{1 - P_I}, \quad (1)$$

that are the inundation probability, the integral time scale and the inundation intermittency, respectively. Figure 4 reports a graphical representation of the procedure described above.

The inundation probability P_I indicates the likelihood that the water level h exceeds the local topography elevation $\eta(x,y)$, defining the fractional time of inundation. The integral time scale τ characterises the stochastic *dichotomic* switching between exposure (dry) and inundation (wet) conditions. It depends on the average duration times of exposure T_e and inundation periods T_i (Ridolfi et al.2011). The lower the τ values, the longer the periods of drought or inundation. The inundation intermittency is strictly related to the inundation probability despite not being confined to the range [0,1]. It is useful for identifying regions at intermediate levels of inundation frequency (corresponding to $\mathcal{I} = \mathcal{O}(1)$). Figure 5a–c compares the three statistical indexes for the reach r6, while the Supporting

TABLE 2 The left column shows the boundary conditions of the 25 simulations to investigate the hydrodynamic behaviour.

ID	Criterion	Modelled		Measured			Visual inspection	
		Flow rate	Water level	Flow rate	Water level	Date	Flow rate	Date
—	___	$(m^3 \cdot s^{-1})$	(m)	$(m^3 \cdot s^{-1})$	(m)		$(m^3 \cdot s^{-1})$	
01	perc. 5	1.2	0.62	1.2	0.48	20/08/2021	/	/
02	perc. 10	2.4	0.67	2.5	0.55	15/04/2021	/	/
03	perc. 15	3.4	0.71	3.4	0.59	17/03/2021	/	/
04	perc. 20	4.4	0.74	4.5	0.63	08/03/2021	/	/
05	perc. 25	5.4	0.77	5.3	0.66	01/03/2021	/	/
06	perc. 30	6.3	0.79	6.4	0.69	03/03/2021	/	/
07	perc. 35	7.4	0.82	7.3	0.71	11/02/2021	/	/
08	perc. 40	8.4	0.84	8.3	0.74	29/05/2021	/	/
09	perc. 45	9.4	0.86	9.3	0.76	31/05/2021	/	/
10	perc. 50	10.5	0.88	10.5	0.79	26/05/2021	10.5	26/05/2021
11	perc. 55	12.1	0.91	11.8	0.81	19/09/2021	/	/
12	perc. 60	14.1	0.94	14.2	0.85	20/05/2021	/	/
13	perc. 65	16.7	0.98	16.7	0.89	25/06/2021	16.7	25/06/2021
14	perc. 70	20.1	1.03	20.7	0.95	10/06/2021	/	/
15	perc. 75	24.2	1.07	23.3	0.99	16/05/2021	/	/
16	perc. 80	29.0	1.13	29.2	1.06	08/10/2020	29.2	08/10/2020
17	perc. 85	35.7	1.20	36.2	1.13	07/10/2020	/	/
18	perc. 90	46.4	1.28	48.7	1.24	13/05/2021	/	/
19	perc. 95	72.0	/	/	/	/	/	/
20	perc. 99	153.0	/	/	/	/	/	/
21	r.t. 1 year	221.0	/	/	/	/	/	/
22	r.t. 2 year	582.0	/	/	/	/	/	/
23	r.t. 5 year	858.0	/	/	/	/	/	/
24	r.t. 10 year	1050.0	/	/	/	/	/	/
25	r.t. 20 year	1240.0	/	/	/	/	/	/

Note: The middle column provides the benchmark values measured at the San Benigno gauging station and used for the first (quantitative) validation. The right column indicates the availability of satellite images for the second (qualitative) validation.
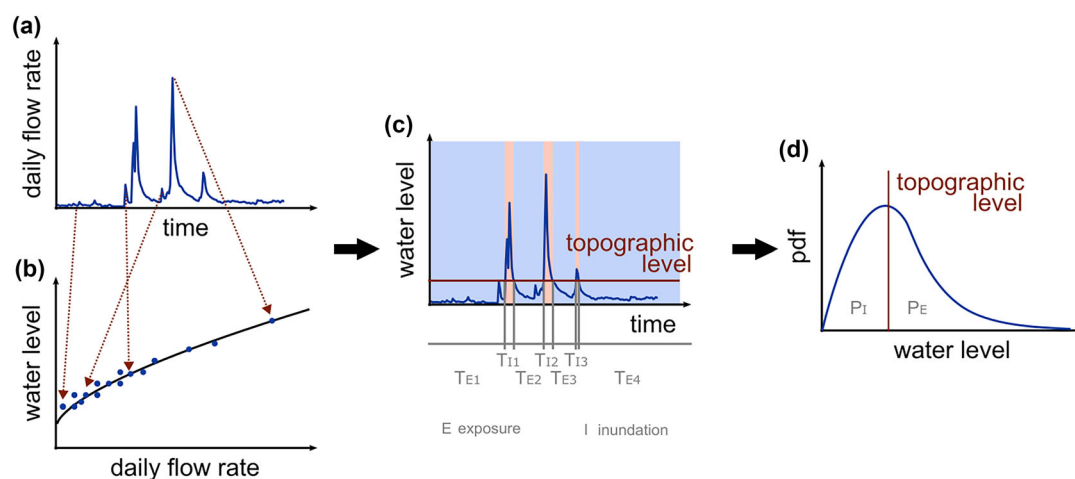

FIGURE 4 Workflow of the computation of the geo-hydrological statistics. Starting from the known time series of discharges (a), a set of hydrodynamic simulations is carried out, and the rating curve relating water levels to flow rates is regressed for each computational cell (b). The water level time series is then generated in each cell (c), and the corresponding probability density function (pdf) is computed (d). From the knowledge of the topography of the investigated cell, the periods of exposure and inundations can be detected and used to calculate their average values (T_E and T_I, respectively) as well as the inundation probability P_I and the probability of exposure $P_E = 1 - P_I$. [Color figure can be viewed at wileyonlinelibrary.com]
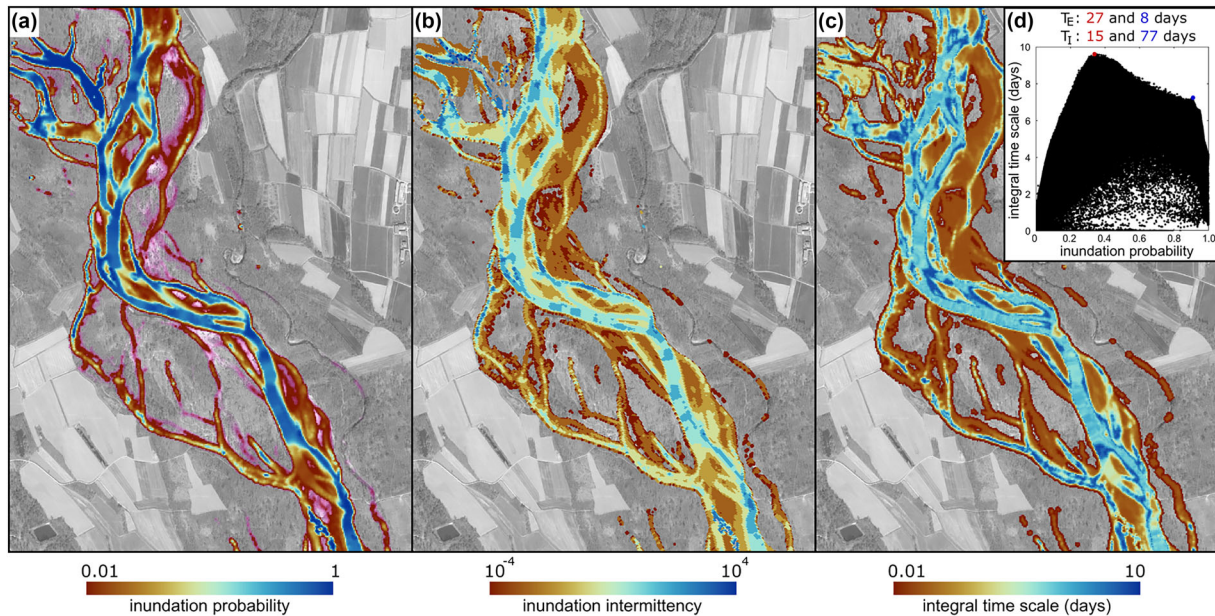
FIGURE 5 (a) Inundation probability, (b) inundation intermittency and (c) integral time scale for a subset of r6. (d) Relationship between the inundation probability and the integral time scale and some illustrative values of T_e and T_i (red and blue points, respectively). [Color figure can be viewed at wileyonlinelibrary.com]

Information provides high-resolution maps of these parameters P_I, τ and $\mathcal{I}$ across the AoI. Notably, a relationship between the hydrological disturbance (represented by the intermittency and the integral time scale) and the percentage occurrence of the floods (represented by the inundation probability) emerges. The integral time scale reaches a plateau at intermediate P_I values (Figure 5d), meaning alternating wet and dry periods of equal duration, namely, a potentially high-stress condition that could challenge vegetation adaptability.

2.6 | Assessment of planform typology and detection of centreline changes

Several endeavours have been recently undertaken to harmonise the morphological classification of rivers using well-defined metrics (Rinaldi et al., 2012). The primary metrics according to this harmonisation are (i) the sinuosity index (Si), indicating the ratio of the total length of the river's centreline to its down-valley length; (ii) the braiding index (Bi), indicating the average number of active channels separated by bars during baseflow conditions; and (iii) the anabranching index (Ai), indicating the average number of active channels separated by vegetated islands during baseflow conditions. Rivers are categorised as transitional (wandering) if their braiding index falls within [1–1.50] and the anabranching index is lower than 1.5.

To ensure the consistency of our classification of Orco's river type with this referenced classification, we calculated the Si, Ai and Bi indexes following the definitions above and the methodology proposed by Rinaldi et al. (2012). In practical terms, we delineated the river centreline in a geographic information system (GIS) system, generated transects at intervals of 250 m (approximately equivalent to the average width of the braid plain), computed the indexes for each reach and assigned the river type according to a lookup table (results in Table 3).

Furthermore, we investigated the slow dynamics of meander migration using the free Matlab tool *River Morphodynamics*

from Analysis of Planforms (RivMAP by Schwenk et al., 2017). This analysis aimed to understand the spatial evolution of the river centreline and detect the most geomorphologically active areas. For each available dataset (i.e., 2019 and 2021), we defined the wet area based on the hydrodynamic simulation related to the mean flow rate and by converting the flood map into a binary image. The tool analysed the Orco River as a single-thread channel by considering the largest envelope in the case of multi-thread reaches.

2.7 | Geomorphic Change Detection (GCD)

To investigate the sudden dynamics related to the flood-induced reactivation of the secondary channels, we employed both satellite imagery analysis and the GCD software (Wheaton et al., 2010; Williams, 2012). The GCD software performs a raster-based comparison of DTMs from different time periods, providing a DTM of difference (DoD) that highlights topographic changes.

When providing input to GCD, potential errors in water-covered areas and the accuracy of the LiDAR-based DTMs must be considered. To mitigate bias and enhance accuracy, we tested four methodological approaches: (M1) using the raw DTMs; (M2) using the raw DTMs but excluding non-vegetated areas; (M3) considering only dry areas; and (M4) using the whole DTM but incorporating bathymetry correction, as described in Section 2.4. The need to test M3 and M4 cases arises from recognising that LiDAR returns may be present in submerged areas, particularly those with shallow water, but those data are unreliable due to spurious reflection from the water surface and/or suspended material.

The noise in the DoD can be handled by applying three filtering options: (F1) *Simple minimum level of detection*, which discards changes in the DoD below a specific absolute threshold; (F2) *Propagated error*, which associates each input DTM with a surface error SE and calculates the final propagated error as

$$FE_{propagated} = \sqrt{SE_{2019}^2 + SE_{2021}^2}; \qquad (2)$$

(F3) *Probabilistic thresholding*, which assesses uncertainty by distinguishing actual changes from white noise in a probabilistic manner. For F1, we set a threshold of 0.250 m, approximately 2.5 times the DTM LiDAR accuracy values. For F2, we applied $SE = 0.125$ m for both the input DTMs, resulting in $FE = 0.175$ m, which is less conservative than the F1 approach. In the case of F3, the final error FE_{prob} is determined using a probabilistic threshold with a certain confidence interval, namely,

$$FE_{probabilistic} = 2t\sqrt{SE_{2019}^2 + SE_{2021}^2}. \qquad (3)$$

In this equation, t is a critical Student's t value at the chosen confidence interval, computed cell-by-cell as a function of the local height of the input DTMs and $FE_{propagated}$ (Wheaton et al., 2010). Setting a confidence interval of 95%, we obtained an average $FE_{probabilistic}$ of 0.340 m.

Using dry DTMs provides accurate information for bare areas (Figure 6b). However, this approach cannot support biogeomorphological analysis in the riparian zone, where wet areas are significant. Conversely, the DoD derived from DTMs fused with the reconstructed bathymetry allows extending the analysis across all areas affected by river disturbance. Despite potential inaccuracies related to the wet channel reconstruction, this approach comprehensively measures the riverbed's change (Figure 6d). Moreover, such

potential inaccuracies might be minimised by applying the probabilistic approach (F3), which proved to be the most conservative one (Figure 6e–h).

In summary, after testing all input options for DTM and DoD computational methods (as shown in the upper and bottom panels in Figure 6, respectively), we opted to analyse the DTMs fused with the reconstructed bathymetry using the probabilistic thresholding method. Additionally, we computed areal and volumetric sediment budgets to quantify the magnitude of erosion and aggradation. We leveraged this information to cross-analyse biogeomorphological processes as explained in Section 2.8.

2.8 | Biomass change detection

We applied the *extended biomass estimation* (EBE) method, as introduced by Latella et al. (2022), to retrieve information concerning the riparian vegetation from the available LiDAR point clouds. This procedure detects individual mature trees based on the three-dimensional properties of the point clouds and combines LiDAR with RGB images to delineate shrubs. The EBE performs segmentation of tree crowns and shrubs by computing individual and areal plant biomass using field-calibrated allometric relationships (further details can be found in the Supporting Information). It also estimates the associated uncertainty in biomass through error propagation. The resulting output consists of the spatial distribution of biomass values. Based on this output, we produced maps and budgets to highlight hotspots of biomass change and quantify the amount involved in riparian dynamics.
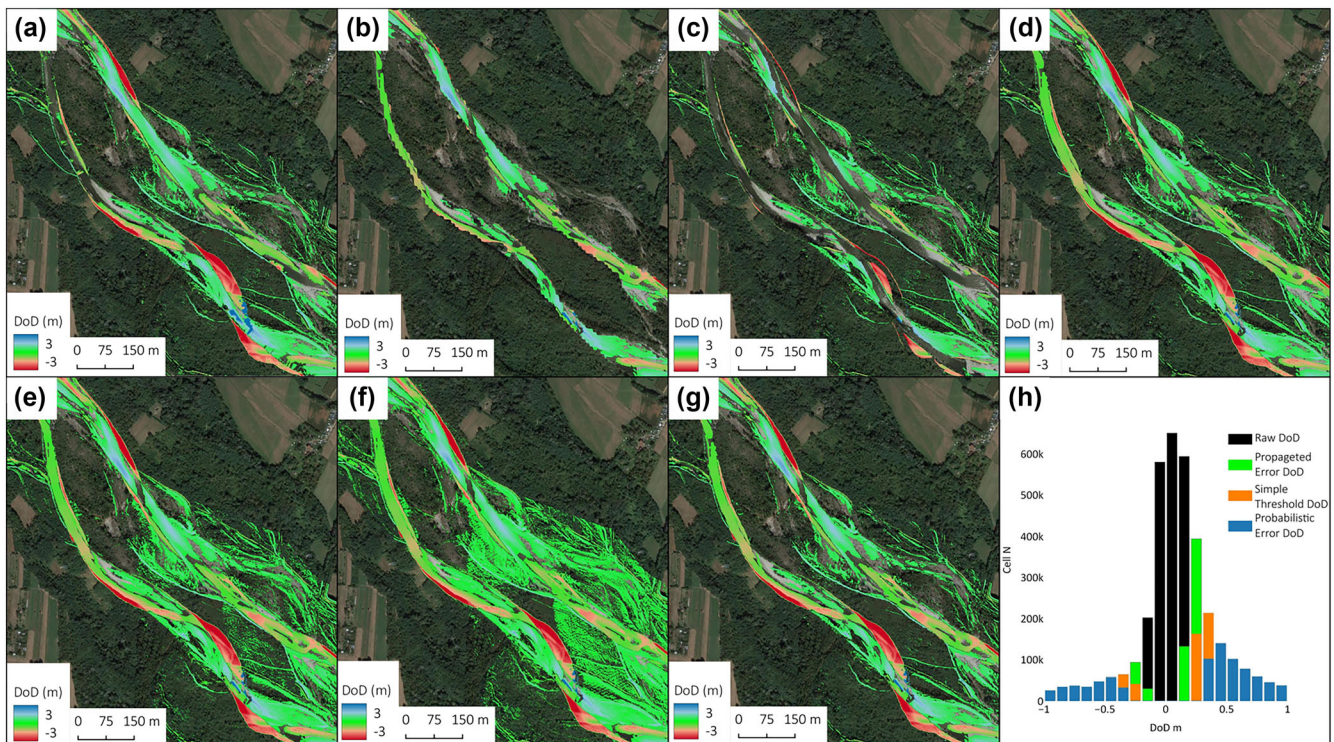

FIGURE 6 In the upper row, the DoDs obtained using the probabilistic method applied to different input DTMs: (a) raw (M1), (b) raw excluding vegetated areas (M2), (c) dry (M3) and (d) fused with reconstructed bathymetry (M4). In the bottom row, examples of results for the different DoD calculation methods offered by GCD software tested with a DTM fused with reconstructed bathymetry: (e) simple threshold (F1), (f) propagated error (F2) and (g) probabilistic error (F3). Panel (h) compares the thresholds associated with the different methods. In all the panels, the shown area belongs to r3. [Color figure can be viewed at wileyonlinelibrary.com]

Finally, we conducted a statistical analysis by cross-referencing topographical and vegetation data to identify any evidence of bio-geomorphological feedback. For this analysis, we subdivided the study site based on the 2019 inundation probability $P_{I,2019}$ (Section 2.5) and considered all the areas with $P_{I,2019} \in [0.1-0.9]$ to avoid including zones with negligible river disturbance ($P_{I,2019}=0$) or enduring wet conditions ($P_{I,2019}=1$). $P_{I,2019}$ values lower than 0.1 are not representative because the domain of $P_{I,2019} \rightarrow 0$ is unbounded, while values with $P_{I,2019} > 0.9$ could be affected by errors related to bathymetry correction and vegetation mapping. Also, we computed the *detrended* elevation η, as the difference between the geodetic elevation of the topography (derived from the georeferenced DTM) and the least-squares fitting plane determined from the point cloud for each reach. The detrended elevation was necessary to remove the mean slope of the river and ensure a more reliable analysis.

3 | RESULTS

3.1 | Planimetric and altimetric evolution of the main channel

The upper reach, r2, is a single-thread channel with few bars. It has braiding and anabranching indexes approximately equal to 1 and, therefore, is classified as sinuous. In contrast, the downstream reaches of the analysed river segment, from r3 to r9, exhibit a more complex geomorphology. Within the reach r3, the Orco River splits into two main channels, where water flows around two stable vegetated islands of significant size and some other active secondary channels separated by bars. In this reach, both the braiding and anabranching indexes largely exceed 1.5, determining anabranching conditions. Within the reaches from r4 to r9, the islands' extension is generally lower than the reach length. Consequently, their presence has a limited impact on the anabranching index, which falls within [1–1.13]. The braiding index is greater than 1.5 for r6 and r7, therefore categorised as braided, while it is lower for r4, r5, r8 and r9, which are classified as wandering.

This classification denotes the prevalent wandering behaviour of the Orco River despite a tendency towards braiding in its central reaches.

From February 2019 to March 2021, the Orco River naturally straightened, with an overall reduction of its centreline length of 2.2% (from 34.7 to 33.9 km) and an increase in slope of 3.6% (from 5.6‰ to 5.8‰). This phenomenon is primarily attributed to a meander cutoff that occurred during the fall 2019 (r8). In this area, the centreline length dropped by 13.6%, the active channel narrowed and the channel direction changed dramatically (Figure 7). The significant variations observed in reach r7 to r9 are due to abrupt modifications during the cutoff and channel adjustment after the events, resulting in a centreline length reduction equal to 5.4% and 2.6% for r7 and r9, respectively. In contrast, the centreline variation remained within ±1.0% in r2 to r6.

The reduction of the centreline length directly impacts the overall sinuosity, whose segment-averaged value changed from 1.35 to 1.32. Also, the variance of the sinuosity notably decreases, indicating a tendency for individual reaches to converge at 1.32. Significant sinuosity variations (r7 to r9) correspond to abrupt morphological changes, that is, meander cutoffs and channel avulsions, as confirmed by the geomorphological analysis (Section 3.2).

Regarding channel width assessment, the RivMAP tool defined the main channel belt by merging wet areas in multi-thread reaches. The resulting channel width for 2019 and 2021 revealed an average decrease (Table 3). The reach r8 experienced the most severe narrowing because the cutoff halved the width of the belt and left an oxbow meander in the floodplain. Only r7 and part of r9 underwent widening because of the reactivation of lateral channels induced by major floods.

We computed the average migration rate as the migrated area divided by the centreline length (Schwenk et al., 2017), with values ranging from 4.95 to 14.77 m·year^{-1} (Table 3) and an average of 10.7 m·year^{-1}. The migration rate per unit width is more uniformly distributed, averaging 0.14 ± 0.05 m·year^{-1} per unit width. Comparing these short-term migration rates with the literature is challenging due to the paucity of similar measurements, especially in countries close to the study area. However, we found an agreement with a previous study on gravel-bed rivers in another part of the Northern Hemisphere (e.g., Nanson & Hickin, 1986).

In general, erosion rates largely exceeded aggradation rates, with r7 and r9 experiencing particularly significant erosion, approximately 11 and seven times the aggradation rates, respectively.
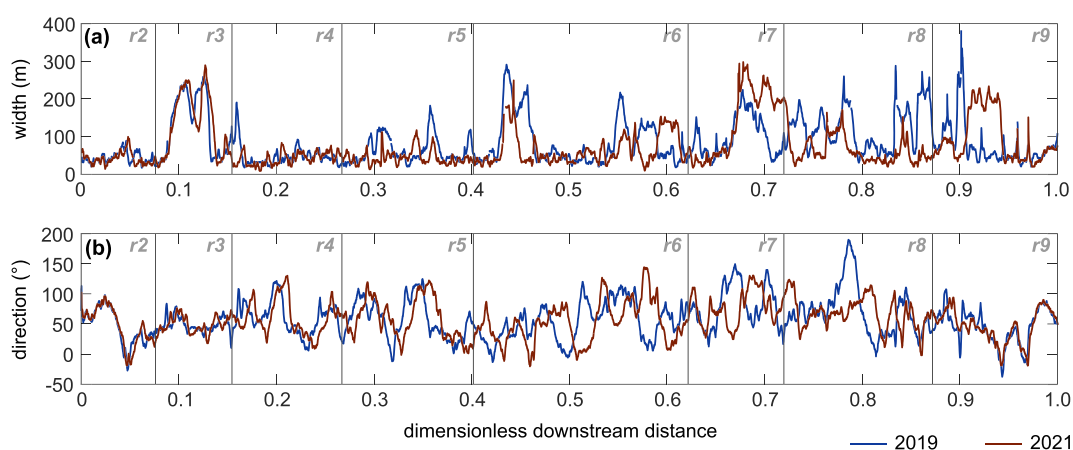

FIGURE 7 Comparison between (a) the main channel width and (b) direction with respect to the centreline direction at the upstream section in 2019 (blue) and 2021 (red). Vertical lines delimitate the reaches (from r2 to r9). [Color figure can be viewed at wileyonlinelibrary.com]

Our analysis highlights a predominant wandering character in the upstream reaches (r2 to r5), where past gravel mining activities continue to induce bed incision and make the river less prone to flood-induced morphological reactivation. In contrast, r6 to r9 represent hotspots of geomorphological change, exhibiting migration rates higher than the overall average and more significant sinuosity variations. Overall, the downstream part of the analysed area is characterised by more intense morphodynamic activity, particularly in terms of erosion and lateral migration.

3.2 | Insights on the morphodynamic evolution

The implementation of the GCD probabilistic method revealed that 21.8% of the AoI was subjected to detectable geomorphic change in 2019–2021. The percentages in the following refer to this *active* area of interest, which we refer to as aAoI. The aAoi has the same longitudinal extension of the AoI but narrower width (0.5 km on average).

Over the 25-month observation period, deposition involved 158.3 ha (54% of the aAoI), while erosion affected 188.4 ha (46%

of the aAoI). Erosion and deposition values per year are reported in Table 4. Although we found a linear relationship between (eroded or aggraded) volumes and areas, we mainly focused on variations in the volume-to-area ratio, namely, the average elevation changes, observing substantial differences between erosion and deposition.

Overall, the eroded volumes were higher than the deposited ones despite areal deposition often exceeding erosion. This indicates that erosion involved relatively smaller areas but high volumes. Looking at the generated DoD and the inundation probability values, we discovered that erosion mainly affected the main channel, indicating that the river has not completely recovered from the tendency to bed degradation. No significant erosion was detected in the floodplain and rarely found in re-opened secondary channels. Most of the erosion affected river banks and terraces. Indeed, the average inundation probability of eroded areas is relatively low (less than 0.65), meaning that the largest contribution of erosion occurs during terrace excavation and collapse during extraordinary floods. In contrast, deposition involved larger areas at a very high probability of inundation, like primary and secondary channels, and promoted new bar formation. Such

TABLE 3 Summary of results of the centreline analysis.

	Average slope		Average width (m)		Sinuosity[a] (m)		Migration rate[b] (m·year^{-1})	Migration rate per unit width (m·m·year^{-1})	Bi	Ai	River type
	2019	2021	2019	2021	2019	2021	2019–2021	2019–2021			
r2	0.0078	0.0078	41.02	39.30	1.27	1.27	4.95	0.12	1.11	1.00	S
r3	0.0092	0.0095	117.83	115.55	1.20	1.19	6.95	0.06	2.90	1.90	A
r4	0.0088	0.0085	47.20	40.92	1.28	1.29	9.39	0.20	1.23	1.08	W
r5	0.0055	0.0060	60.14	42.32	1.32	1.32	8.50	0.14	1.37	1.12	W
r6	0.0048	0.0047	79.43	63.61	1.32	1.31	14.77	0.19	1.67	1.41	B
r7	0.0035	0.0035	93.18	135.35	1.37	1.29	12.55	0.13	1.58	1.08	B
r8	0.0028	0.0034	113.98	59.58	1.49	1.29	11.65	0.10	1.42	1.11	W
r9	0.0028	0.0031	90.71	88.19	1.37	1.34	13.36	0.15	1.37	1.06	W
All	0.0056	0.0058	80.43	73.10	1.35	1.32	10.26 ± 3.38	0.14 ± 0.05	-	-	Mostly W

Abbreviations: A, anabranching; Ai, anabranching index; B, braided; Bi, braiding index; S, sinuous; W, wandering.
[a]The sinuosity (or sinuosity index) is computed as the ratio between the total centreline and down-valley length.
[b]The average migration rate is computed as the migrated area per centreline length.

TABLE 4 Summary of results of the DoD analysis.

| ID	Area/year (m^3·year^{-1})		Volume/year (^{3}·year^{-1})		Volume/area/year (m·year^{-1})		Volume/centreline length (m·km^{-1}·year^{-1})	
	Erosion	Deposition	Erosion	Deposition	Erosion	Deposition	Erosion	Deposition
r2	39 960	45 463	44612 ± 7064	30229 ± 8037	0.54	0.32	17 183	11 644
r3	54 900	85 486	64564 ± 9705	64631 ± 15112	0.57	0.37	23 091	23 115
r4	67 869	86 785	83008 ± 11998	74852 ± 15341	0.59	0.41	20 995	18 933
r5	73 736	128 880	70305 ± 13035	86778 ± 22783	0.46	0.32	15 505	19 135
r6	171 102	258 031	188378 ± 30247	170675 ± 45614	0.53	0.32	24 659	22 341
r7	69 935	94 551	74493 ± 12363	61407 ± 16714	0.51	0.31	22 053	18 178
r8	167 215	107 713	214129 ± 29560	83486 ± 19041	0.62	0.38	39 553	15 418
r9	116 413	98 991	131877 ± 20579	67812 ± 17500	0.54	0.33	28 284	14 543
Overall	761 128	905 901	871367 ± 53131	639870 ± 63845	0.54 ± 0.05	0.34 ± 0.04	25 106	18 438
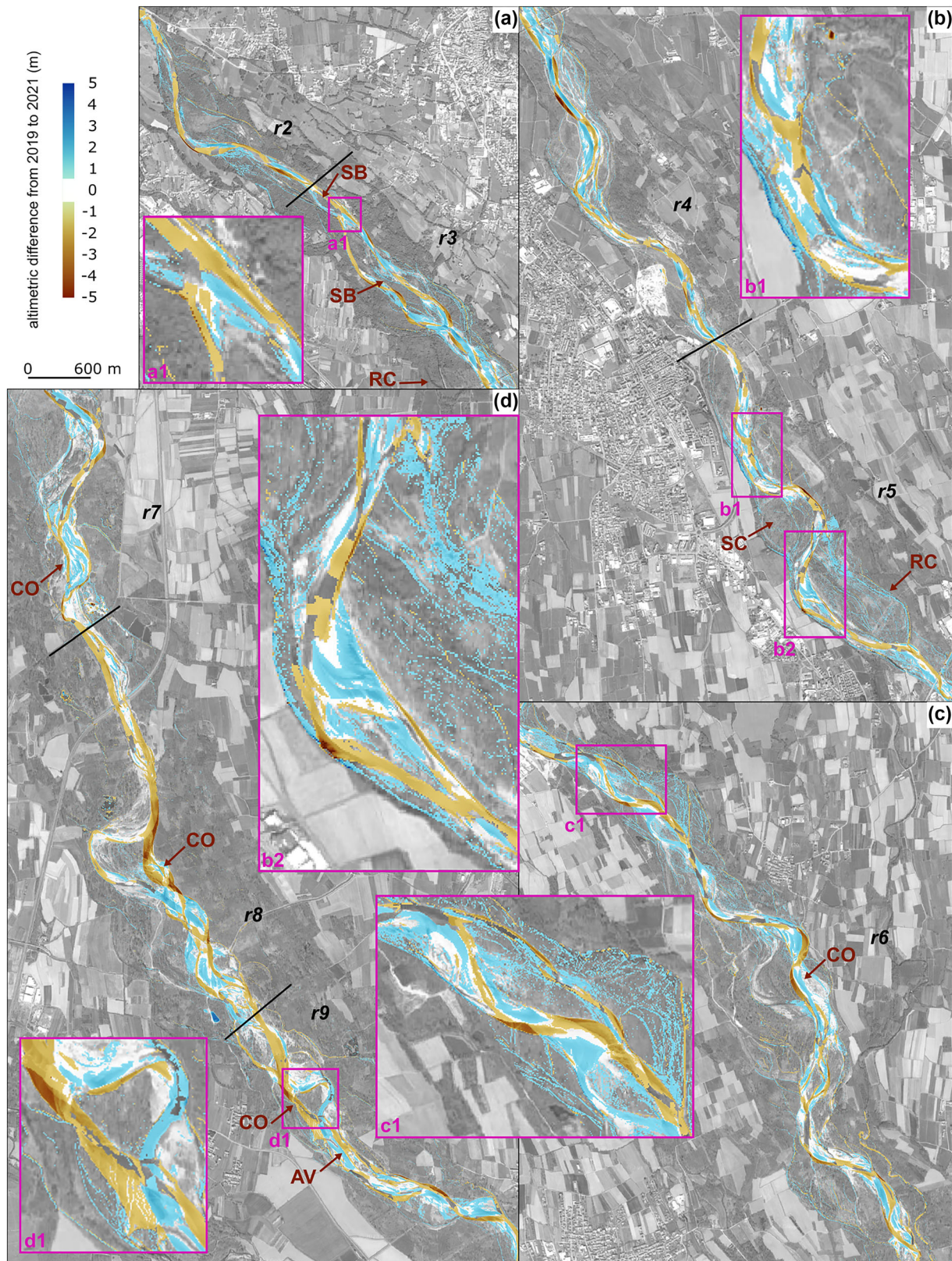
FIGURE 8 Dem of Difference (DoD) from 2019 to 2021 across the area of interest: (a) reaches 2 and 3, (b) 4 and 5, (c) 6 and (d) 7 to 9. Additional zoom-in across the main morphological changes: (a_1) upstream bar accretion, (b_1,d_1) meander cutoff and (b_2,c_1) channel avulsion. Labels indicate the major morphological features, like avulsions (AV), meander cutoffs (CO), reactivated channels (RC) and stable bifurcations (SB). [Color figure can be viewed at wileyonlinelibrary.com]

a tendency to bar formation agrees with other observations reported in the literature highlighting sedimentation after severe floods and during ordinary flows in several cross-sections of the Orco River (Surian, Rinaldi, et al., 2009; Turitto et al.2010).

Notably, the volume-to-area ratio is approximately a constant value of 0.33 m·year^{-1} for deposition and 0.54 m·year^{-1} for erosion (Table 4) across all the reaches, albeit each of them responded differently to the hydro-morphological forcing.

In the upstream part of the AoI, planimetry of the single-thread channel is characterised by severe bed degradation, accompanied by moderate bar dynamics. Specifically, reach r2 experienced overall sediment loss with erosion exceeding deposition (Figure 8a).

In r3, we noted an alternation between single- and multi-thread planimetry, exhibiting wandering behaviour, moderate channel migration and a balanced gain-to-loss sediment budget. In this reach, the presence of abandoned meanders prone to reactivation during major floods (labelled as RC in Figure 8a) recalls past migration of the river channels. In addition, bifurcations are remarkably stable, in agreement with the upstream bar accretion detected by the DoD analysis (labelled as SB in Figure 8a$_1$) and previous field observations on bifurcations (Burge, 2006). This stability in bifurcations was noteworthy despite the short-term monitoring period.

The river is definitively wandering in r4, characterised by intense lateral migration and bar dynamics and, again, a tendency towards sediment loss. In r5, the Orco River exhibits high morphological activity. Previous lateral migration was accompanied by pulsing reactivation of the secondary channel network. During the rising limb of flooding events, some secondary channels were temporarily reactivated and then filled with sediments during the recession limb, resulting in net aggradation (labelled as RC in Figure 8b).

In r5, the Alex storm in October 2020 triggered a meander chute cutoff (Figure 8b$_1$) due to the final enlargement of a swale that served as a preferential routing path during previous floods (Constantine et al., 2010). Furthermore, the same event induced a sudden channel avulsion downstream of the cutoff (Figure 8b$_2$). The river shifted from the primary channel to a secondary one and then significantly widened. Notably, the avulsion might have been promoted by human activities. Zooming on the orthophotos (not shown in the figure), small artificial transversal chutes connecting the primary and secondary channels are evident. These were likely dredged for water supply needs after the main channel had moved away from the crop fields in the floodplain.

Channel abandonment also occurred in r6 (Figure 8c$_1$), which had the highest migration rate. Satellite image analysis indicated the presence of a swale channel that could have triggered a natural chute meander cutoff (labelled as CO in Figure 8c), which occurred between February and September 2019. However, no significant enlargements of a pre-existing channel were recorded. Also, a flood-driven unstable bifurcation (sensu Burge, 2006) was observed in this reach.

In r8, meander migration was moderate until October 2019, when two consecutive 2-year return time events led to a dramatic enlargement of a pre-existing chute channel (as reported in Figure 1d) and the consequent meander cutoff (labelled as CO in Figure 8d). The initial chute was narrower than 10 m before the cutoff and wider than 30 m 16 months later. The abandoned meander currently conveys only a negligible residual flow. Upstream the cutoff, the riverbed experienced up to 4.0 m of incision.

Reaches r7 and r9 underwent channel reconfiguration, including cutoffs and downstream channel avulsions, labelled as CO and AV in Figure 8d. Extensive chute enlargement occurred during the 2-year return time flood on 24 October 2019, followed by complete abandonment of the main channel during the subsequent 2-year return time flood (24 November 2019). In the brief period between these two events (1 month), water flow excavated the chute channel and induced the downstream sections to meander, preparing the river for

the cutoff during the subsequent flood (Figure 8d$_1$). Artificial secondary channels, likely used for agricultural purposes, facilitated this latter cutoff.

Overall, it emerges that, in the upstream sections of the Orco River, where it is sinuous and single thread, there is a net export of sediment from the main channel to the downstream sections. In contrast, the downstream wandering and braided multi-thread sections move part of the received sediment and their bed-excavated sediment towards lateral bars and the surrounding floodplain. The remaining sediment exits the study site, meaning that it is received from the Po River at the confluence with the Orco River.

3.3 | Insights on the biomass response to river disturbance

The EBE tool allowed us to describe the spatio-temporal dynamics of riparian biomass, shedding light on the processes that hinder vegetation growth and survival within the AoI. Furthermore, the tool provided a biomass difference (BD) raster (Figure 9). The BD map allowed us to identify three main processes related to biomass dynamics. Two of these processes mirror the duality of the Orco River's behaviour, while a third process is of anthropogenic origin: (i) the slow but continuous scouring causing root exposure on riverbanks; (ii) the intermittent occurrence of mechanical stress during floods on the floodplain and along banks; and (iii) the vegetation removal due to human activities, like dirt road enlargement or farming.

Overall, the comparative analysis of EBE results between 2019 and 2021 indicates that vegetation growth compensated for disturbances caused by both human activities and river processes (Table 5). Despite the transitional behaviour of the Orco River, characterised by generalised morphological reactivation during extreme events and an overall shrinking of vegetated areas of −6%, the biomass remarkably grew in all the reaches with a net increase of 35%. In particular, biomass density increased from 344 to 499 Mg·ha^{-1}. These values, referring to fresh biomass, are consistent with the literature that reports [20–500] Mg·ha^{-1} as the typical range for dry biomass of riparian shrubs and trees in temperate areas (Cartisano et al., 2013; Huylenbroeck et al., 2021; Rheinhardt et al., 2012). It is worth noting that any differences among the literature values and the study site depend on the complex interplay between plant productivity, which is influenced by environmental disturbance and resources, and their features, such as age and species (Camporeale et al., 2013; Corenblit et al., 2007; Huylenbroeck et al., 2021; Naiman & Decamps, 1997; Osterkamp et al., 2012).

The increase in biomass reflects a resilience that is partly attributed to the high adaptability of pioneer riparian vegetation, which is able to withstand river disturbance through an enhanced growth rate during its early stages, promoting bar encroachment (Bowman et al., 2013; Caudullo & de Rigo, 2016; Corenblit et al., 2014; Salerno et al., 2023; Tabacchi et al., 2009). Moreover, vegetation benefited from the reactivation of the secondary channel network and the restored lateral connectivity. In the following paragraphs, the different processes leading to biomass increase are analysed thoroughly.

In the upstream single-thread section (e.g., r2), the predominant disturbance was vegetation removal caused by bank erosion. Here, an increase in biomass was promoted by the concurrence of two
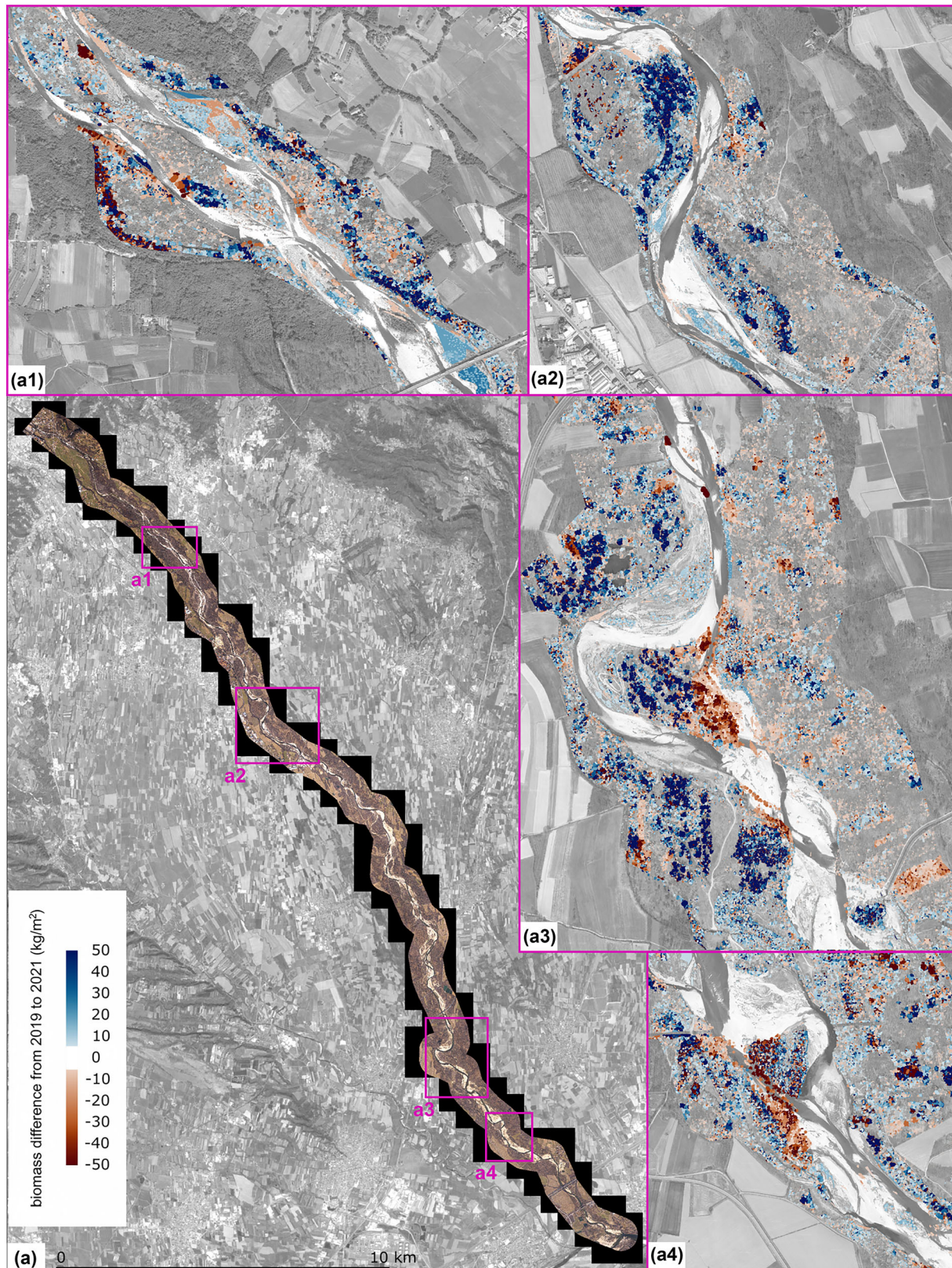
FIGURE 9 (a) Orthophoto of the areo of interest in 2019. Additional panels zoom across the biomass difference (BD) map to show the main biomass changes: (a₁) mature vegetation removal during palaeo-channel reactivation and boosted growth along secondary channels, (a₂) overall growth thanks to increased connectivity and (a₃,a₄) extensive removal caused by cutoffs. [Color figure can be viewed at wileyonlinelibrary.com]

processes. First, as mentioned in Section 3.2, the river bed degraded significantly despite little lateral erosion, resulting in negligible direct uprooting due to overflow. Second, bed incision was not so severe to induce floodplain–waterflow disconnection or generate harsh conditions for vegetation dynamics.

Where the transitional character of the Orco River is particularly pronounced (r3 and r6) and lateral migration is significant, vegetated areas notably shrunk. The most intense biomass loss occurred within palaeo-channels (Figure 9a₁), whose pulse reactivation caused the removal of mature trees. Biomass loss was also severe across eroded

TABLE 5 Summary of results of the biomass budget analysis.

ID	Biomass (Mg)			Vegetated area (ha)		
	2019	**2021**	**% Difference**	**2019**	**2021**	**% Difference**
2	7107.7 ± 585.0	9308.8 ± 839.6	+31.0	42.5	41.0	−3.6
3	14848.1 ± 1351.8	20203.0 ± 1428.1	+36.1	48.0	42.5	−11.5
4	6456.3 ± 241.6	10952.5 ± 745.3	+69.6	30.0	29.2	−2.7
5	14294.8 ± 164.7	27967.7 ± 1483.3	+95.6	57.8	59.3	2.5
6	67591.8 ± 1391.1	87055.0 ± 3196.1	+28.8	155.5	134.8	−13.3
7	21249.1 ± 748.2	23182.4 ± 1166.1	+9.1	74.1	70.2	−5.3
8	47296.5 ± 1457.8	70531.5 ± 2561.3	+49.1	150.5	141.7	−5.9
9	41070.8 ± 1677.4	49027.3 ± 1740.5	+19.4	80.5	78.5	−2.5
All	219915.1 ± 3112.7	298228.2 ± 5163.8	+35.6	639.1	597.3	−6.5

bars, although it was outbalanced by the generation of new bare areas suitable for vegetation encroachment. Thus, despite causing sudden vegetation removal due to slow and fast flood dynamics, transitional patterns promote the natural restoration of lateral connectivity. Boosted vegetation growth along secondary channels reflects the improved conditions related to network reactivation (see r3, r5 and r6, Figure 9b,c). In some areas, the overall growth during the observation period led to a doubling of vegetation biomass, albeit some areas were evidently subjected to loss (e.g., r5). This phenomenon is likely because the predominance of lateral migration, rather than bed incision, maintains floodplain connectivity, favouring optimal nutrient and soil moisture conditions. Moreover, some areas with high lateral migration rates did not experience biomass loss because the river wandered across almost bare bars. In general, we noticed that wandering and braided sections can self-heal, meaning they can naturally recover their lateral connectivity (Fryirs & Brierley, 2016).

In the reaches where the river is wandering for ordinary floods, vegetation has no time to grow. This is the case for r7, where we observed the smallest growth. Here, the relatively high inundation probability over the bars prevented plants from establishing and reaching the maturity needed to withstand mechanical drag. This means that the window of opportunity (WoO) for successful establishment rarely took place (Caponi et al., 2019).

As described above, during the observation period, some meander cutoff occurred (e.g., within r8 and r9, reducing the channel length from about 1700 to 990 m and from about 820 to 460 m, respectively). In these areas, vegetation removal was primarily caused by the enlargement of the pre-existing chute channel, while the floodplain areas farther from the chute benefited from a reduction in inundation probability. Despite undergoing extensive morphological changes, r8 experienced one of the most remarkable increases in vegetation biomass (+49%).

Finally, it is worth noting that, despite low anthropogenic disturbance being one of the criteria to define the AoI, some areas undeniably show evidence of vegetation removal due to human activities (e.g., vehicle passage in the upper part of r4 and logging in the lower part of r6). Also, we remark that the extended biomass detection performed in this work is a powerful tool, but it cannot discriminate the age, structure and species composition of riparian vegetation. An improved approach should combine the present one with the identification of the year of colonisation from historical aerial maps, along with forestry information, as recently done by Godfroy et al. (2023) on Ain River (France).

4 | DISCUSSION

This section explores some fundamental processes and general features emerging from a complex biogeomorphological scenario. We investigated this scenario starting from the integrated quantitative analysis presented in the preceding sections, emphasising the relationships among the factors composing the bio-hydro-geomorphological triad.

4.1 | The signature of vegetation

Previous studies (Bertoldi et al., 2011) have identified the signature of vegetation on the riparian topography by observing that (i) a Gamma distribution can fit the topographical distribution across a river reach and its surrounding floodplain and (ii) the presence of tall and dense vegetation is indicated by secondary peaks in the probability density function (pdf). These findings paved the way for the systematic use of topographic elevation as a descriptor for vegetation dynamics (Bertoldi et al., 2011; Camporeale et al., 2013; Gurnell & Grabowski, 2016; Gurnell et al., 2001) and as a key parameter in biogeomorphological modelling (Camporeale & Ridolfi, 2006, 2007; Camporeale et al., 2013; Muneepeerakul et al., 2007; Vesipa et al.2015).

We tested these findings on our data by examining the pdf of the detrended elevation η for all the computational cells within our study sites (Figure 10a). Notably, apart from the trivial shift of the pdf corresponding to vegetated areas towards higher elevations (+0.5 m), we did not observe other qualitative differences in the shapes of the two distributions. Consequently, in the present case, there is no statistical evidence in favour of a *Gamma*- over than a *Gaussian*-like shape.

Subsequently, we supposed that the disturbance influencing vegetation distribution can be attributed not only to topography but also to water level fluctuations. Thus, we generated histograms of the inundation probability P_I (Figure 10b) to ascertain our hypothesis. We discovered that the pdf for all cells (vegetated and not) comprises a declining curve at lower values of P_I and a second mode at higher
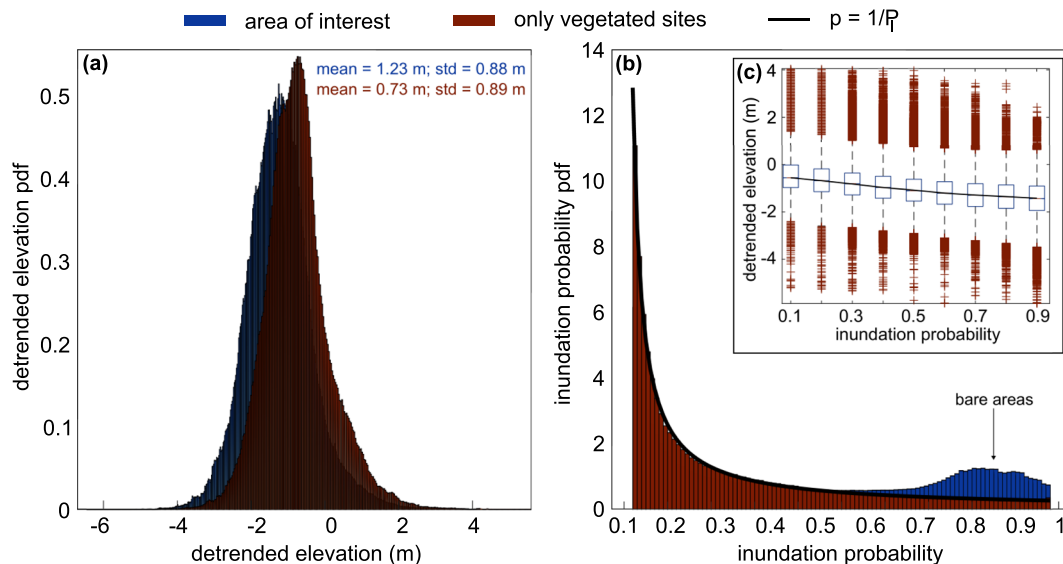
FIGURE 10 Probability density functions (pdf) of (a) the *detrended* elevation η and (b) inundation probability P_I. Blue and red histograms represent the whole area of interest and the vegetated sites, respectively. (c) Linkage between topography and inundation probability. [Color figure can be viewed at wileyonlinelibrary.com]

values. This latter mode corresponds to frequently inundated *bare* areas because it is completely absent in the pdf of the vegetated sites. Remarkably, it can be shown that, when considering P_I, the pdf of vegetated sites p_{veg} closely follows the analytic function

$$p_{veg} = \frac{N}{P_I} \quad \left(\text{with} N^{-1} = \log \frac{P_{I,max}}{P_{I,min}} \right), \tag{4}$$

where the normalisation constant N allows for a unit area in the range $P_I = [P_{I,min}, P_{I,max}]$ (see the black curve in Figure 10b). By setting $P_{I,min} = 2\%$ and $P_{I,max} = 98\%$, it follows that $N \sim 1/4$ and, therefore, $p_{veg} \sim (4P_I)^{-1}$. We statistically assessed the accuracy of this result for each reach. The absolute error between the empirical and theoretical distributions falls within the range [6% to 15%]. The theoretical distribution $p_{veg} = N/P_I$ has a mean $\overline{P_I} = 0.267$ and a standard deviation $\sigma_{P_I} = 0.250$, which are consistent with the empirical values of the whole sample ($\overline{P_I} = 0.241$, $\sigma_{P_I} = 0.249$, resulting in a coefficient of variation $c_v = \sigma_{P_I}/\overline{P_I}$ of approximately 1).

It is worth noting that, from a statistical perspective, there is an inverse relationship between η and P_I (i.e., high inundation probability corresponds to lower sites on average, see Figure 10c). Nevertheless, our findings demonstrate that P_I is more effective in detecting bare planforms (hidden in the tail of the distribution), in particular when secondary channels enhance connectivity. While Bertoldi et al. (2011) proved that riparian tree growth moderates the morphological aspect of braided rivers, we found that in the presence of vegetation biomass, the hydro-morphological disturbance, summarised by the inundation probability P_I, exhibits a typical signature. This conclusion does not invalidate the previous hypothesis but broadens the spectrum of factors considered in biogeomorphological studies.

Considering η may be more straightforward for preliminary assessments (i.e., its computation does not require any hydrodynamic simulations), which likely explains its widespread use in the literature. However, our work revealed that P_I assumes a typical shape in vegetated riparian sites, which can be described with a simple analytical

relationship. Consequently, P_I can be recognised as a stronger descriptor of riparian vegetation biogeography (Figure 11), capturing the interplay between spatial vegetation biomass distribution and patterns of physical factors (i.e., topography and water level-induced stress). For this reason, we adopted it throughout the biogeomorphological analysis reported in the following paragraphs.

We remark that our findings trigger further theoretical interpretations based on minimalistic mathematical models. These approaches for river biogeomorphology and ecohydrology usually rely on the stochastic modelling of the dichotomic switching between the growth and decay states of riparian vegetation (see, e.g., Camporeale & Ridolfi, 2006; Latella et al., 2020; Vesipa et al., 2015). One crucial feature of the dichotomic noise is the inundation probability. Thus, the present observations build a bridge between theoretical frameworks and real data and could inspire the search for exponential-like solutions of the master equation for the vegetated state. However, this goes beyond the objectives of the present study, so we leave further investigation to forthcoming works.

4.2 | Biomass gain and loss and carbon storage

Transitional rivers, here classified as wandering, are characterised by a dual behaviour that significantly influences biomass dynamics. In theory, where wandering rivers act as predominantly single-thread channels with spurious island bifurcations and under stable morphological conditions, vegetation has the chance to adapt over time (Peixoto et al., 2009). Consequently, vegetation can continuously adjust to morphological changes, leading to a neutral biomass balance (i.e., gain-to-loss ratio close to one, meaning carbon neutrality). However, in the case of the Orco River, we observed a gain-to-loss ratio in the range [1.5–2.5], with a mean value of 1.8 ± 0.4 (Figure 11a), indicating a tendency for biomass growth and carbon storage. Although the relatively short observation period (25 months) is not sufficient for any definitive conclusion about sediment and biomass budgets, it can provide
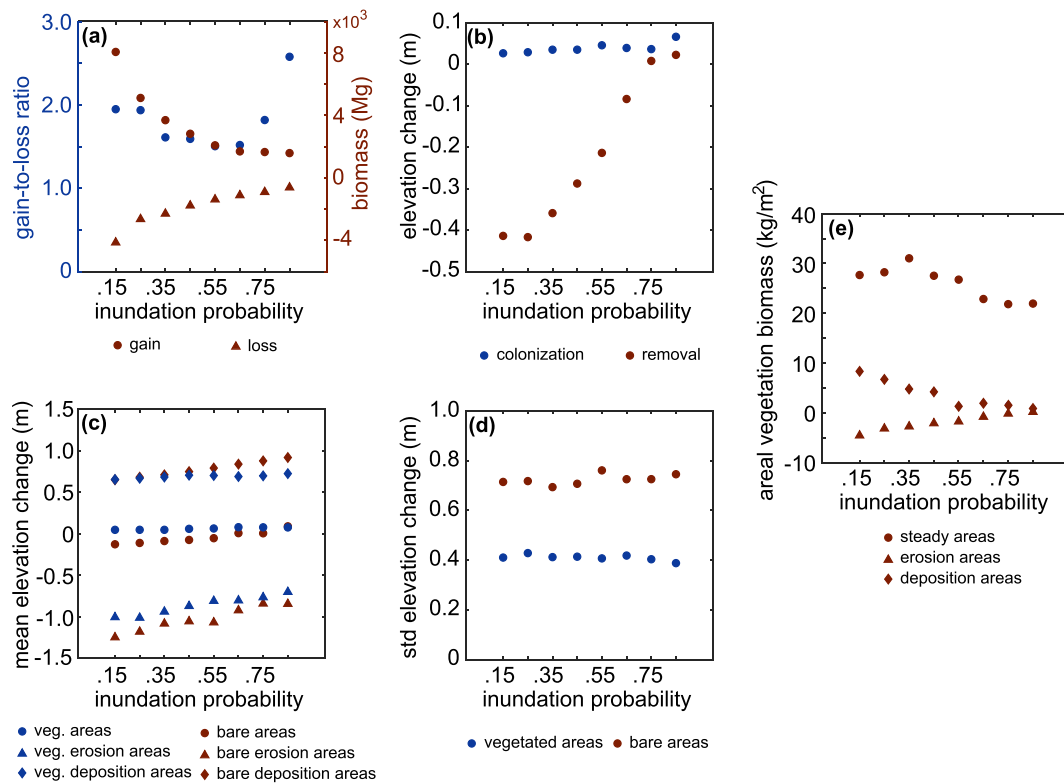
FIGURE 11 (a) The biomass gain-to-loss ratio and the amount of gained and lost biomass for increasing inundation probability values. (b) The trend of (detrended) elevation change associated with vegetation establishment removal. The trend of (c) mean and (d) standard deviation morphological change associated with erosion and deposition in bare and vegetated areas. (e) The trends of areal biomass changes in steady, eroded and aggraded areas for increasing inundation probability values. [Color figure can be viewed at wileyonlinelibrary.com]

information about the rare events that occurred during this period (October 2019, November 2019 and October 2020, with return periods equal 2, 2 and 20 years, respectively).

The gain-to-loss ratio shows a low variability across areas regardless of their inundation probabilities P_I, and its value depends on different processes occurring at the various P_I areas. A separate analysis of biomass loss and gain allowed us to uncover the physical processes at play in zones with different P_I. At low P_I values (i.e., far from the river or on terraces), biomass gain was high (Figure 11a). Here, vegetation benefited from low hydro-morphodynamic disturbance caused by channel deepening, although the low connectivity of terraces also meant reduced nutrient import and a deeper water table. Thus, in this case, beneficial effects exceeded adverse dynamics. Biomass gain was partly compensated by the dramatic removal of mature trees during flood-induced reactivation of secondary and palaeo-channels and bank erosion. Moreover, although we excluded the urbanised areas and crop fields from the analysis, some of the biomass loss at low P_I values might be attributable to other anthropogenic activities, such as dirt road enlargement and wood harvesting. At higher P_I values, both biomass gain and loss decreased because low-biomass plants (shrubs and young trees belonging to Salicaceae species, black locusts, European oaks and hornbeams, as described in Section 2.1) predominate near the main channel. This led to relatively little biomass changes during the windows of opportunity and little loss during floods. For intermediate disturbance levels, the detrimental role of hydro-morphological river dynamics seemed to be outbalanced by benefits (e.g., nutrients and moisture supply).

Previous studies demonstrated that the riparian bio-geomorphological feedback leads to a carbon-neutral budget (Peixoto et al., 2009) or a net flux from the floodplain to the water flow (Walcker et al., 2021). In contrast, our results reveal that in cases far from equilibrium, that is the case of the Orco River characterised by a significant bed degradation, dramatic random river migration pulses and overflows, the short-term gain-to-loss ratio is larger than one. Such value suggests positive feedback between floodplain reworking and vegetation growth. Also, this value means that, despite the high hydro-morphological disturbance, riparian vegetation recovers, benefiting from river dynamics in the short term. Part of biomass gain can be attributed to (i) the formation of bare soil, which provides spaces for vegetation encroaching, and (ii) the rapid growth of pioneer riparian species in the early phases of their life cycle (Hupp, 1992; Mahoney & Rood, 1998; Gurnell et al., 2001; Corenblit et al., 2014; Latella et al., 2022; Salerno et al., 2023). However, the most significant process seems to be linked to sudden channel shifts, as illustrated by the BD reported in Figure 9a₃ for an emblematic case of meander cutoff occurred during the study period. In this case, although significant vegetation removal (indicated by reddish colours) near the chute due to the widening of the existing channel, several areas benefited from the planform reconfiguration. For instance, intermediate and mature vegetation on scroll bars in the point bars (just upstream of the cut and in the meander) experienced less disturbance from ordinary overflow after the cutoffs, resulting in a net gain in biomass (highlighted by light to dark blue colours in the same figure).

4.3 | The correlation between biomass and topographic changes

In areas where P_I < 0.75, vegetation removal was related to sediment entrainment and soil erosion. Conversely, removal occurred in those areas experiencing aggradation (Figure 11b). In the former case, the loss of plants was caused by their phenological death or their uprooting during major floods. Indeed, the uprooting of a tree is generally associated with the excavation of a block of ground containing a large part of the root system (Calvani et al., 2019), therefore causing the lowering of the ground level. In the latter case, it is worth recalling that (i) the removal of vegetation during floods might be followed by sediment deposition once the flood ends and (ii) the observed removal of vegetation might also involve plants that are buried during the formation of new bars (Gurnell et al.2001).

On average, bare soil was closer to the main channel than vegetated areas (mean P_I 0.55 vs 0.36). This is likely due to the capability of vegetation to withstand river disturbance unless its magnitude and frequency become too high, as observed in areas with relatively high inundation probability.

Comparing erosion and deposition across vegetated and bare areas, it emerges that a slight overall net aggradation occurred in vegetated areas (blue circles in Figure 11c), as commonly expected (Bywater-Reyes et al., 2022; Camporeale et al., 2013; Edwards et al., 1999; Nanson & Beach, 1977; Osterkamp et al., 1998). However, examining erosion and deposition individually reveals that both erosion and deposition rates were lower in vegetated areas than in bare ones (diamonds vs triangles in Figure 11c). Furthermore, the presence of vegetation reduced the standard deviation of the vertical topographical changes (Figure 11d), likely because the root system establishes a typical scale in the excavation process. These results denote the role of vegetation in controlling geomorphological processes in a manner that induces damping of topographic change with respect to the non-vegetated case.

Erosion generally led to biomass loss (triangles in Figure 11e). We observe higher loss for lower P_I, indicating the root excavation of older trees far from the active channel due to flood-induced reactivation of secondary channels or palaeo-channels. Notably, for P_I higher than 0.75, erosion was associated with biomass gain, likely showing the encroachment of pioneer vegetation across new bare areas after the *cleaning* action of floods removing the armoured soil layer or grass cover. In contrast, deposition only occured in areas of overall biomass gain, despite a small gain at higher P_I (diamonds in Figure 11e). From a reverse perspective, the higher the areal vegetation density—mature vegetation is found far from the active channel according to riparian ecological succession—the higher the sediment trapping capability and, therefore, aggradation.

We notice some dissimilarities between the trends of BDs in morphologically steady areas found in this work (circles in Figure 11e) and the overall shape of the carrying capacity provided by the literature (as summarised by Camporeale & Ridolfi, 2006; Latella et al., 2020). The literature on the riparian zone reports a biomass peak corresponding to site-specific optimal soil moisture conditions, typically indicating intermediate–low disturbance, in agreement with the findings of previous studies relating stochastic noise (i.e., random hydrological fluctuations) and vegetation dynamics (Ridolfi et al., 2011). In contrast, we found the maximum biomass increment at small

P_I values, probably because the wandering behaviour of the Orco River promotes the connectivity of floodplains ($P_I \rightarrow 0$), boosting vegetation growth, in particular near the reactivated channels.

4.4 | A focus on colonisation

Colonisation is a crucial issue in fluvial biogeomorphology because it still needs to be properly decoded. We leveraged the short interval between the two LiDAR acquisitions to delve into it.

Particularly, we investigated the magnitude and distribution of colonisation by narrowing our datasets to the sites with zero biomass in 2019 and non-zero biomass in 2021. We found out that the ratio between the area of colonised sites over the potentially colonisable region in 2019 (i.e., all sites in the AoI with T_r < 20 years and P_I < 0.95) amounts to 0.61%, which is equivalent to a colonisation rate of 0.3% per year ($\sim$500 m$^2 \cdot$ km^{-1} of centreline length per year). Also, plant establishment was always associated with slight sediment deposition (Figure 11d), which is equal to 5 ± 3 cm (about 2.4 cm·year^{-1}), and the relationship between the topographical vertical change and the vegetation removal is almost linear.

Although we demonstrated the superiority of the inundation probability, with respect to the detrended topographic elevation, in describing vegetation distribution and biomass loss and gain, we also noticed that the inundation probability alone is not sufficient to discriminate mature vegetation from colonisation sites. Therefore, we explored the potential of other descriptors for colonisation by performing a principal component analysis (PCA) on the following variables: P_I, τ, the detrended elevation η, the maximum, the mean and the 99th percentile of the bed shear stress ($\tau_{sb}^{max}, \overline{\tau_{sb}}, \tau_{sb,95}$), along with a novel parameter given by the product between the mean bed shear stress $\overline{\tau_{sb}}$ and the average duration of inundation period T_I. This new parameter takes into account the persistence of the detrimental effect of high water levels on germination. Because this variable has the units similar to viscosity [Pa·d instead of Pa·s]. We remind that, to compute this latter quantity, T_i must be derived by manipulating the relationship in (1), obtaining $T_i = \tau/(1 - P_I)$. Consequently, Γ is given by

$$\Gamma = \frac{\tau}{1 - P_I} \overline{\tau_{sb}}, \quad (5)$$

where $\overline{\tau_{sb}}$ is the temporal average of the mean shear stress in the cell during the inundation periods, while τ is the integral scale.

As Figure 12a shows, the shear stress, especially its maximum value, plays a dominant role, likely because germination and seedling survival are possible only when drag forces remain below a certain threshold. This observation agrees with previous studies (Dixon & Turner, 2006; Mahoney & Rood, 1998; Oorschot et al., 2016; Zhu et al., 2023). However, when adding the Γ parameter to the analysis, Γ assumes a leading role (Figure 12b), being four-fold more effective in describing the dataset of the colonised sites (i.e., the variance associated to the principal component increased four times). This underscores that the inundation viscosity Γ is an excellent proxy for the detection of colonisation sites. Notably, when T_i or T_e is considered individually, they do not play a significant role as descriptors.

To further validate such a result, we conducted a comparative analysis among reaches by comparing the 95th percentile of Γ
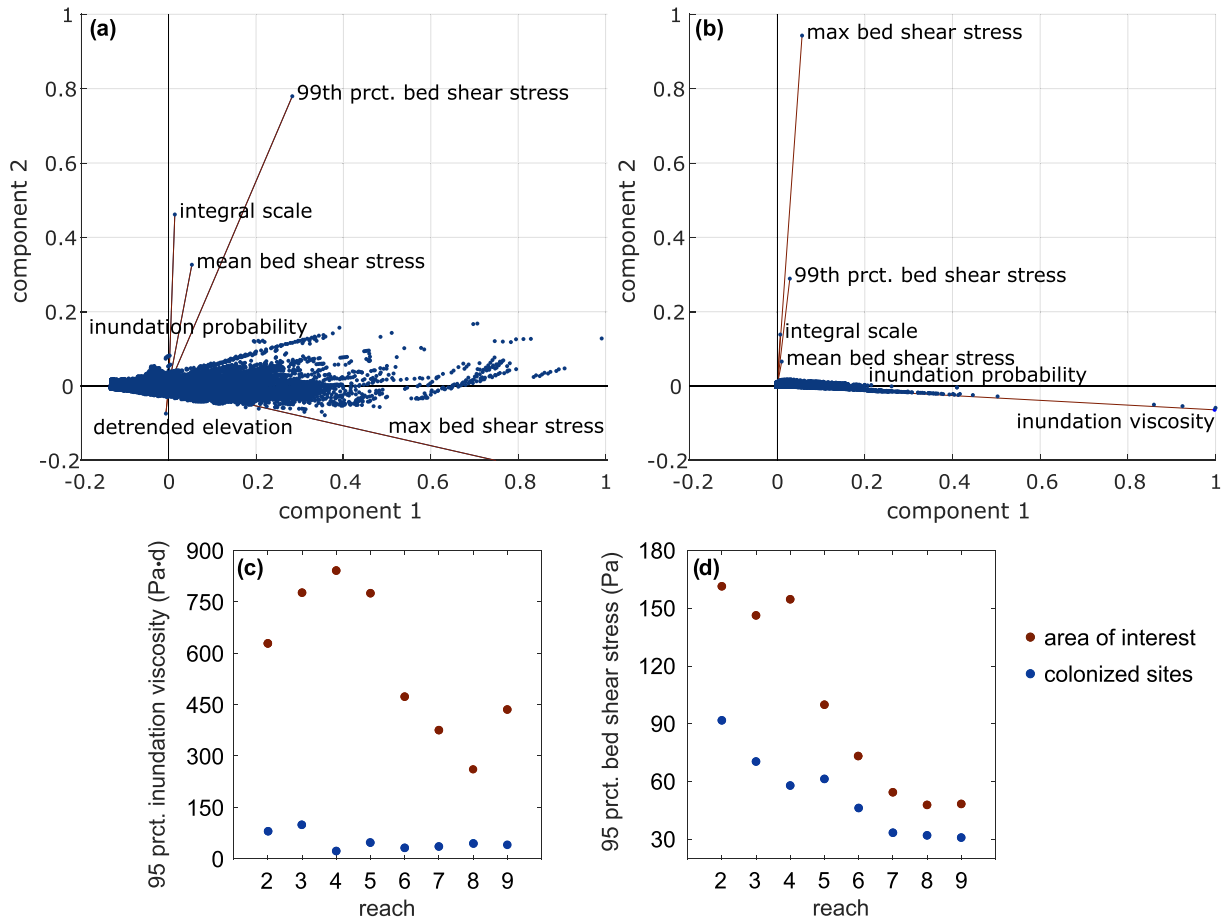
FIGURE 12 PCA biplots projected on the first two principal components considering all the variables (inundation probability P_I, integral scale τ, detrended elevation η, the maximum, the mean and the 99th percentile of the bed shear stress τ_{sb}^{max}, $\overline{\tau_{sb}}$ and $\tau_{sb,95}$) except for (a) and including (b) the inundation viscosity Γ. Comparison of the 95th percentile of Γ (c) and τ_{sb}^{max} (d) between the entire area of interest (red dots) and the colonised cells only (blue dots). [Color figure can be viewed at wileyonlinelibrary.com]

(Figure 12c) and τ_{sb}^{max} (Figure 12d) between colonised cells and the whole AoI. The results highlight that the adoption of an upper threshold Γ_{th} as a condition for colonisation is quite unequivocal and independent from the different geomorphological settings of the reach, which is not the case when considering τ_{sb}^{max}. In conclusion, a reliable criterion for plant establishment is given by $\Gamma < \Gamma_{th}$, where, based on the used dataset, $\Gamma_{th} \sim 70$ Pa·d. This indication could support parameter setting in biogeomorphological modelling of the riparian zone (e.g., Caponi et al., 2020; Oorschot et al., 2016) or for defining the WoO for germination, as conceptualised by Balke et al. (2014).

5 | CONCLUSIONS

Remote sensing of rivers has grown rapidly since the 2000s, answering the need for low-cost, multi-temporal, spatially extended data to investigate the spatio-temporal evolution of river systems. The present work attempted to go one step further by integrating remote sensing with field surveys and hydrodynamic modelling. This multi-disciplinary approach allowed us to unveil some biogeomorphological processes occurring across a transitional gravel-bed river.

Our geomorphological assessment confirmed the prevailing wandering behaviour of the Orco River, albeit observing the tendency to braid in some reaches. We detected hotspots of intense morphodynamic activity corresponding to the braided reaches and the downstream wandering reaches. The presence of these hotspots indicates an occurring flood-induced morphological reactivation of the past Orco braided conditions. Furthermore, the analysis also highlighted the predominance of erosion rather than deposition and the redistribution of sediments from the riverbed to lateral bars, inducing a multi-thread pattern. Thus, we expect a potential increase in the braiding and anabranching indexes of the downstream reaches in the near future.

Exploring vegetation dynamics, we recorded a net increase in biomass during the observation periods and despite the high disturbance of floods. As commented above, this increase has several causes besides vegetation resilience. In some areas, sudden channel shifts, avulsions or meander cutoffs promote partial disconnection, allowing other regions with intermediate or mature vegetation to be less disturbed from uprooting during successive ordinary flows. In others, self-heal of lateral connectivity was observed, as the river wandering improved soil moisture and nutrient conditions for vegetation survival while generating new room for plant encroachment. Accordingly, we observed that (i) erosion was not related to biomass loss as usual in highly frequently inundated areas, but it promoted a slight biomass gain, and (ii) the maximum biomass increment did not occur at intermediate–low disturbance as reported by the literature but closer

to the active and reactivated channels. These processes indicate that, differently from the long-term neutrality of carbon budget in the floodplain of meandering rivers, transitional rivers induce carbon storage in the shape of vegetation biomass thanks to their short-term morphological instability and the different timescales between vegetation and morphological adjustments. We remark that this process would not have been detected if the integrated approach was not adopted.

Cross-analysis among our bio-, hydro- and morphological data also proved the interplay between hydro-morphological conditions and vegetation dynamics and our hypothesis that hydro-morphological variables can provide robust descriptors for vegetation distribution. First, while previous studies found a signature of vegetation on topography only, we identified a signature on the hydro-morphological conditions, summarised by the inundation probability P_I. Indeed, the P_I probability density function follows an exponential distribution depending on P_I in the vegetated areas, while, in the other areas, it has an additional mode indicating bare bars. Second, we observed that the variance of vertical topographical changes, both for erosion and aggradation, was definitely lower in vegetated areas rather than in bare ones, likely indicating a typical scale in morphological processes induced by plant root systems. Third, we identified a new parameter, called inundation viscosity, that can discriminate the conditions allowing plant establishment. This parameter is given by the product of the mean bed shear stress and the average duration of inundation, summarising the impacts of high water levels on vegetation. Future research will address the test of this parameter across other rivers and its implementation into existing riparian bio-geomorphological models.

CONFLICT OF INTEREST STATEMENT

The authors declare that the research was conducted in the absence of any commercial or financial relationships that could be construed as a potential conflict of interest.

DATA AVAILABILITY STATEMENT

The LiDAR datasets used in the present work are available upon request to the corresponding author. The described algorithms are openly available. The RivMAP tool can be found at https://it.mathworks.com/matlabcentral/fileexchange/58264-rivmap-river-morphodynamics-from-analysis-of-requestedDomain=, while the Geomorphic Change Detection (GCD) software and the Extensive Biomass Estimation (EBE) algorithm at https://gcd.riverscapes.net/ and https://github.com/MelissaLatella/EBE_Extended_Biomass_Estimation, respectively.

ORCID

Melissa Latella https://orcid.org/0000-0003-3678-6992
Davide Notti https://orcid.org/0000-0002-8256-0743
Marco Baldo https://orcid.org/0000-0001-9841-0531
Daniele Giordan https://orcid.org/0000-0003-0136-2436
Carlo Camporeale https://orcid.org/0000-0002-7311-6018

REFERENCES

ARPA (2019a) Eventi idro-meteorologici dal 19 al 24 Ottobre 2019. Parte I, Agenzia Regionale per la Protezione Ambientale—Piemonte Event report.

ARPA (2019b) Eventi idro-meteorologici dal 22 al 25 Novembre 2019., Agenzia Regionale per la Protezione Ambientale—Piemonte Event report.

ARPA (2020) Eventi alluvionali in Piemonte. Evento del 2-3 Ottobre 2020, Agenzia Regionale per la Protezione Ambientale—Piemonte.

ARPA (2021) Monitoraggio della qualit delle acque in Piemonte. Available from: https://webgis.arpa.piemonte.it/monitoraggio_qualita_acque_mapseries/monitoraggio_qualita_acque_webapp/

Baldo, M., Bicocchi, C., Chiocchini, U., Giordan, D. & Lollino, G. (2009) LIDAR monitoring of mass wasting processes: the Radicofani landslide, Province of Siena, Central Italy. Geomorphology, 105(3-4), 193–201.

Balke, T., Herman, P.M.J. & Bouma, T.J. (2014) Critical transitions in disturbance-driven ecosystems: identifying windows of opportunity for recovery. Journal Ecology, 102(3), 700–708.

Baptist, M.J., Babovic, V., Rodríguez Uthurburu, J., Keijzer, M., Uittenbogaard, R.E., Mynett, A. & Verwey, A. (2007) On inducing equations for vegetation resistance. Journal of Hydraulic Research, 45(4), 435–450.

Bendix, J. & Stella, J.C. (2022) Riparian vegetation and the fluvial environment: a biogeographic perspective. In Treatise on geomorphology. Amsterdam, The Netherlands: Elsevier; 298–319.

Bertoldi, W., Gurnell, A.M. & Drake, N.A. (2011) The topographic signature of vegetation development along a braided river: results of a combined analysis of airborne lidar, color air photographs, and ground measurements. Water Resources Research, 47(6), W06525.

Best, J. (2019) Anthropogenic stresses on the world's big rivers. Nature Geoscience, 12(1), 7–21.

Bizzi, S., Piégay, H., Demarchi, L., Van de Bund, W., Weissteiner, C.J. & Gob, F. (2019) LiDAR-based fluvial remote sensing to assess 50–100-year human-driven channel changes at a regional level: the case of the Piedmont Region, Italy. Earth Surface Processes and Landforms, 44(2), 471–489.

Bowman, D.M.J.S., Brienen, R.J.W., Gloor, E., Phillips, O.L. & Prior, L.D. (2013) Detecting trends in tree growth: not so simple. Trends in Plant Science, 18(1), 11–17.

Brown, A.G., Lespez, L., Sear, D.A., Macaire, J.-J., Houben, P., Klimek, K., Brazier, R.E., Van Oost, K. & Pears, B. (2018) Natural vs anthropogenic streams in Europe: history, ecology and implications for restoration, river-rewilding and riverine ecosystem services. Earth-Science Reviews, 180, 185–205.

Burge, L.M. (2006) Stability, morphology and surface grain size patterns of channel bifurcation in gravel–cobble bedded anabranching rivers. Earth Surface Processes and Landforms: The Journal of the British Geomorphological Research Group, 31(10), 1211–1226.

Bywater-Reyes, S., Diehl, R.M., Wilcox, A.C., Stella, J.C. & Kui, L. (2022) A green new balance: interactions among riparian vegetation plant traits and morphodynamics in alluvial rivers. Earth Surface Processes and Landforms, 47(10), 2410–2436.

Calvani, G., Francalanci, S. & Solari, L. (2019) A physical model for the uprooting of flexible vegetation on river bars. Journal of Geophysical Research: Earth Surface, 124(4), 1018–1034.

Camporeale, C., Laio, F., Sola, F., Vezza, P. & Maschio, P. (2021) Attivit di supporto tecnico scientifico alla progettazione definitiva di opere di gestione dei sedimenti del torrente Orco, Politecnico di Torino Technical report.

Camporeale, C., Perucca, E., Ridolfi, L. & Gurnell, A.M. (2013) Modeling the interactions between river morphodynamics and riparian vegetation. Reviews of Geophysics, 51(3), 379–414.

Camporeale, C. & Ridolfi, L. (2006) Riparian vegetation distribution induced by river flow variability: a stochastic approach. Water Resources Research, 42(10), W10415.

Camporeale, C. & Ridolfi, L. (2007) Noise-induced phenomena in riparian vegetation dynamics. *Geophysical Research Letter*, 34(18), L18406.

Caponi, F., Koch, A., Bertoldi, W., Vetsch, D.F. & Siviglia, A. (2019) When does vegetation establish on gravel bars? Observations and modeling in the Alpine Rhine river. *Frontiers in Environmental Science*, 7, 124.

Caponi, F., Vetsch, D.F. & Siviglia, A. (2020) A model study of the combined effect of above and below ground plant traits on the ecomorphodynamics of gravel bars. *Scientific Reports*, 10(1), 1–14.

Cartisano, R., Mattioli, W., Corona, P., Mugnozza, G.S., Sabatti, M., Ferrari, B., Cimini, D. & Giuliarelli, D. (2013) Assessing and mapping biomass potential productivity from poplar-dominated riparian forests: a case study. *Biomass and Bioenergy*, 54, 293–302.

Cassardo, C., Loglisci, N., Paesano, G., Rabuffetti, D. & Qian, M.W. (2006) The hydrological balance of the October 2000 flood in Piedmont, Italy: quantitative analysis and simulation. *Physical Geography*, 27(5), 411–434.

Caudullo, G. & de Rigo, D. (2016) Populus tremula in Europe: distribution, habitat, usage and threats. In *European atlas of forest tree species*, Luxembourg: Publications Office of the EU.

Comiti, F., Da Canal, M., Surian, N., Mao, L., Picco, L. & Lenzi, M.A. (2011) Channel adjustments and vegetation cover dynamics in a large gravel bed river over the last 200 years. *Geomorphology*, 125(1), 147–159.

Constantine, J.A., McLean, S.R. & Dunne, T. (2010) A mechanism of chute cutoff along large meandering rivers with uniform floodplain topography. *Geological Society of America Bulletin*, 122(5–6), 855–869.

Corenblit, D., Steiger, J., González, E., Gurnell, A.M., Charrier, G., Darrozes, J., Dousseau, J., Julien, F., Lambs, L. & Larrue, S. (2014) The biogeomorphological life cycle of poplars during the fluvial biogeomorphological succession: a special focus on Populus nigra L. *Earth Surface Processes and Landforms*, 39(4), 546–563.

Corenblit, D., Tabacchi, E., Steiger, J. & Gurnell, A.M. (2007) Reciprocal interactions and adjustments between fluvial landforms and vegetation dynamics in river corridors: a review of complementary approaches. *Earth-Science Reviews*, 84(1-2), 56–86.

D'Alpaos, A., Toffolon, M. & Camporeale, C. (2016) Ecogeomorphological feedbacks of water fluxes, sediment transport and vegetation dynamics in rivers and estuaries. *Advance in Water Resources*, 93, 151–155.

Dawson, M., Gurnell, A. & Lewin, J. (2022) Biogeomorphic recovery of a river reach affected by mining. *Earth Surface Processes and Landforms*, 47(15), 3497–3514.

Demarchi, L., Bizzi, S. & Piégay, H. (2017) Regional hydromorphological characterization with continuous and automated remote sensing analysis based on VHR imagery and low-resolution LiDAR data. *Earth Surface Processes and Landforms*, 42(3), 531–551.

Dixon, M.D. & Turner, M.G. (2006) Simulated recruitment of riparian trees and shrubs under natural and regulated flow regimes on the Wisconsin River, USA. *River Research and Applications*, 22(10), 1057–1083.

Downs, P.W. & Piégay, H. (2019) Catchment-scale cumulative impact of human activities on river channels in the late Anthropocene: implications, limitations, prospect. *Geomorphology*, 338, 88–104.

Dufour, S., Rinaldi, M., Piégay, H. & Michalon, A. (2015) How do river dynamics and human influences affect the landscape pattern of fluvial corridors? Lessons from the Magra River, Central–Northern Italy. *Landscape and Urban Planning*, 134, 107–118.

Edmaier, K., Burlando, P. & Perona, P. (2011) Mechanisms of vegetation uprooting by flow in alluvial non-cohesive sediment. *Hydrology and Earth System Sciences*, 15(5), 1615–1627.

Edwards, P.J., Kollmann, J., Gurnell, A.M., Petts, G.E., Tockner, K. & Ward, J.V. (1999) A conceptual model of vegetation dynamics on gravel bars of a large Alpine river. *Wetlands Ecology and Management*, 7, 141–153.

Fryirs, K.A. & Brierley, G.J. (2016) Assessing the geomorphic recovery potential of rivers: forecasting future trajectories of adjustment for use in management. *Wiley Interdisciplinary Reviews: Water*, 3(5), 727–748.

Garófano-Gómez, V., Metz, M., Egger, G., Díaz-Redondo, M., Hortobágyi, B., Geerling, G., Corenblit, D. & Steiger, J. (2017) Vegetation succession processes and fluvial dynamics of a mobile temperate riparian ecosystem: the lower Allier River (France). *Géomorphologie: Relief, Processus, Environnement*, 23(3), 187–202.

Godfroy, J., Lejot, J., Demarchi, L., Bizzi, S., Michel, K. & Pigay, H. (2023) Combining hyperspectral, LiDAR, and forestry data to characterize riparian forests along age and hydrological gradients. *Remote Sensing*, 15(1), 17.

Gregory, K.J. (2006) The human role in changing river channels. *Geomorphology*, 79(3–4), 172–191.

Gurnell, A. (2014) Plants as river system engineers. *Earth Surface Processes and Landforms*, 39(1), 4–25.

Gurnell, A.M. & Grabowski, R.C. (2016) Vegetation–hydrogeomorphology interactions in a low-energy, human-impacted river. *River Research and Applications*, 32(2), 202–215.

Gurnell, A.M., Petts, G.E., Hannah, D.M., Smith, B.P.G., Edwards, P.J., Kollmann, J., Ward, J.V. & Tockner, K. (2001) Riparian vegetation and island formation along the gravel-bed Fiume Tagliamento, Italy. *Earth Surface Processes and Landforms*, 26(1), 31–62.

Hupp, C.R. (1992) Riparian vegetation recovery patterns following stream channelization: a geomorphic perspective. *Ecology*, 73(4), 1209–1226.

Hupp, C.R. & Osterkamp, W.R. (1996) Riparian vegetation and fluvial geomorphic processes. *Geomorphology*, 14(4), 277–295.

Huylenbroeck, L., Latte, N., Lejeune, P., Georges, B., Claessens, H. & Michez, A. (2021) What factors shape spatial distribution of biomass in riparian forests? Insights from a LiDAR survey over a large area. *Forests*, 12(3), 371.

Karim, F., Dutta, D., Marvanek, S., Petheram, C., Ticehurst, C., Lerat, J., Kim, S. & Yang, A. (2015) Assessing the impacts of climate change and dams on floodplain inundation and wetland connectivity in the wet–dry tropics of northern Australia. *Journal of Hydrology*, 522, 80–94.

Kayitesi, N.M., Guzha, A.C. & Mariethoz, G. (2022) Impacts of land use land cover change and climate change on river hydro-morphology—a review of research studies in tropical regions. *Journal of Hydrology*, 615, 128702.

Langat, P.K., Kumar, L. & Koech, R. (2019) Monitoring river channel dynamics using remote sensing and GIS techniques. *Geomorphology*, 325, 92–102.

Latella, M., Bertagni, M.B., Vezza, P. & Camporeale, C. (2020) An integrated methodology to study riparian vegetation dynamics: from field data to impact modeling. *Journal of Advances in Modeling Earth Systems*, 12(8), e2020MS002094.

Latella, M., Raimondo, T., Belcore, E., Salerno, L. & Camporeale, C. (2022) On the integration of LiDAR and field data for riparian biomass estimation. *Journal of Environmental Management*, 13(2), 322.

Latella, M., Sola, F. & Camporeale, C. (2021) A density-based algorithm for the detection of individual trees from LiDAR data. *Remote Sensing*, 13(2), 322.

Liébault, F. & Piégay, H. (2002) Causes of 20th century channel narrowing in mountain and piedmont rivers of southeastern France. *Earth Surface Processes and Landforms: The Journal of the British Geomorphological Research Group*, 27(4), 425–444.

Lollino, G., Nigrelli, G. & Audisio, C. (2005) Bacino idrografico del Torrente Orco: analisi integrata evento-fenomeno-danno. *Quaderni di Geologia Applicata*, 12(1), 49–62.

Maaß, A.-L., Schüttrumpf, H. & Lehmkuhl, F. (2021) Human impact on fluvial systems in Europe with special regard to today's river restorations. *Environmental Sciences Europe*, 33, 1–13.

Mahoney, J.M. & Rood, S.B. (1998) Streamflow requirements for cottonwood seedling recruitment: an integrative model. *Wetlands*, 18, 634–645.

Martínez-Fernández, V., Van Oorschot, M., De Smit, J., González del Tánago, M. & Buijse, A.D. (2018) Modelling feedbacks between geomorphological and riparian vegetation responses under climate change in a Mediterranean context. *Earth Surface Processes and Landforms*, 43(9), 1825–1835.

Messerli, B., Grosjean, M., Hofer, T., Nunez, L. & Pfister, C. (2000) From nature-dominated to human-dominated environmental changes. *Quaternary Science Reviews*, 19(1–5), 459–479.

Molau, U. (2008) On the interface between ecology and geomorphology. *Norsk Geografisk Tidsskrift-Norwegian Journal of Geography*, 62(2), 52–54.

Muneepeerakul, R., Rinaldo, A. & Rodriguez-Iturbe, I. (2007) Effects of river flow scaling properties on riparian width and vegetation biomass. *Water Resources Research*, 43(12), W12406.

Naiman, R.J. & Decamps, H. (1997) The ecology of interfaces: riparian zones. *Annual Review of Ecology and Systematics*, 28(1), 621–658.

Nanson, G.C. & Beach, H.F. (1977) Forest succession and sedimentation on a meandering-river floodplain, northeast British Columbia, Canada. *Journal of Biogeography*, 1977, 229–251.

Nanson, G.C. & Hickin, E.J. (1986) A statistical analysis of bank erosion and channel migration in western Canada. *Geological Society of America Bulletin*, 97(4), 497–504.

Nigrelli, G. & Audisio, C. (2010) Floods in Alpine river basins (Italy): an interdisciplinary study combining historical information and hydroclimatic data. *Geografia Fisica e Dinamica Quaternaria*, 33(2), 205–213.

Nilsson, C., Reidy, C.A., Dynesius, M. & Revenga, C. (2005) Fragmentation and flow regulation of the world's large river systems. *Science*, 308(5720), 405–408.

Notebaert, B. & Verstraeten, G. (2010) Sensitivity of West and Central European river systems to environmental changes during the Holocene: a review. *Earth-Science Reviews*, 103(3–4), 163–182.

O'Briain, R. (2019) Climate change and European rivers: an eco-hydromorphological perspective. *Ecohydrology*, 12(5), e2099.

Oorschot, M., Kleinhans, M., Geerling, G. & Middelkoop, H. (2016) Distinct patterns of interaction between vegetation and morphodynamics. *Earth Surface Processes and Landforms*, 41(6), 791–808.

Osterkamp, W.R., Hupp, C.R. & Stoffel, M. (2012) The interactions between vegetation and erosion: new directions for research at the interface of ecology and geomorphology. *Earth Surface Processes and Landforms*, 37(1), 23–36.

Osterkamp, W.R., Scott, M.L. & Auble, G.T. (1998) Downstream effects of dams on channel geometry and bottomland vegetation: regional patterns in the Great Plains. *Wetlands*, 18(4), 619–633.

Peña, F. & Nardi, F. (2018) Floodplain terrain analysis for coarse resolution 2D flood modeling. *Hydrology*, 5(4), 52.

Peixoto, J.M.A., Nelson, B.W. & Wittmann, F. (2009) Spatial and temporal dynamics of river channel migration and vegetation in central Amazonian white-water floodplains by remote-sensing techniques. *Remote Sensing of Environment*, 113(10), 2258–2266.

Pellegrini, L., Maraga, F., Turitto, O., Audisio, C., Duci, G., Pavia, U. & Ferrata, V. (2008) Evoluzione morfologica di alvei fluviali mobili nel settore occidentale del bacino padano. *Italian Journal of Quaternary Sciences*, 21(1b), 251–266.

Rheinhardt, R.D., Brinson, M.M., Meyer, G.F. & Miller, K.H. (2012) Carbon storage of headwater riparian zones in an agricultural landscape. *Carbon Balance and Management*, 7, 1–5.

Ridolfi, L., D'Odorico, P. & Laio, F. (2011) *Noise-induced phenomena in the environmental sciences*. Cambridge: Cambridge University Press.

Rinaldi, M. (2003) Recent channel adjustments in alluvial rivers of Tuscany, Central Italy. *Earth Surface Processes and Landforms: The Journal of the British Geomorphological Research Group*, 28(6), 587–608.

Rinaldi, M., Surian, N., Comiti, F., Bussettini, M., Belletti, B., Nardi, L., Lastoria, B. & Golfieri, B. (2012) *IDRAIM—stream hydromorphological evaluation, analysis and monitoring system. Guidebook for the evaluation of stream morphological conditions by the Morphological Quality Index (MQI). Version 1.1*. Rome: ISPRA.

Rodríguez-González, P.M., Abraham, E., Aguiar, F., Andreoli, A., Baležientienè, L., Berisha, N., Bernez, I., Bruen, M., Bruno, D. & Camporeale, C. (2022) Bringing the margin to the focus: 10 challenges for riparian vegetation science and management. *Wiley Interdisciplinary Reviews: Water*, 9(5), e1604.

Rosso, M., Comino, E., Fresia, I. & Dutto, F. (2008) Programma generale di gestione dei sedimenti (PGS) per i corsi d'acqua piemontesi. programma di gestione dei sedimenti per il torrente Orco, Agenzia Interregionale per il fiume PO and Politecnico di Torino Technical report.

Roux, C., Alber, A., Bertrand, M., Vaudor, L. & Piégay, H. (2015) "FluvialCorridor": a new ArcGIS toolbox package for multiscale riverscape exploration. *Geomorphology*, 242, 29–37.

Rumsby, B.T. & Macklin, M.G. (1994) Channel and floodplain response to recent abrupt climate change: the Tyne basin, Northern England. *Earth Surface Processes and Landforms*, 19(6), 499–515.

Salerno, L., Moreno-Martinez, Izquierdo-Verdiguier, E., Clinton, N., Siviglia, A. & Camporeale, C. (2022) Satellite analyses unravel the multi-decadal impact of dam management on tropical floodplain vegetation. *Frontiers in Environmental Science*, 10, 871530.

Salerno, L., Vezza, P., Perona, P. & Camporeale, C. (2023) Eco-morphodynamic carbon pumping by the largest rivers in the Neotropics. *Scientific Report*, 13(1), 5591.

Schwenk, J., Khandelwal, A., Fratkin, M., Kumar, V. & Foufoula-Georgiou, E. (2017) High spatiotemporal resolution of river planform dynamics from Landsat: the RivMAP toolbox and results from the Ucayali River. *Earth and Space Science*, 4(2), 46–75.

Scorpio, V. & Piégay, H. (2021) Is afforestation a driver of change in Italian rivers within the Anthropocene era? *Catena*, 198, 105031.

Surian, N. & Rinaldi, M. (2003) Morphological response to river engineering and management in alluvial channels in Italy. *Geomorphology*, 50(4), 307–326.

Surian, N., Rinaldi, M., Pellegrini, L., Audisio, C., Maraga, F., Teruggi, L., Turitto, O. & Ziliani, L. (2009) Channel adjustments in northern and central Italy over the last 200 years. In *Management and restoration of fluvial systems with broad historical changes and human impacts*, Vol. 451, Boulder, CO: Geological Society of America; 83–95.

Surian, N., Ziliani, L., Comiti, F., Lenzi, M.A. & Mao, L. (2009) Channel adjustments and alteration of sediment fluxes in gravel-bed rivers of North-Eastern Italy: potentials and limitations for channel recovery. *River Research and Applications*, 25(5), 551–567.

Tabacchi, E., Steiger, J., Corenblit, D., Monaghan, M.T. & Planty-Tabacchi, A.-M. (2009) Implications of biological and physical diversity for resilience and resistance patterns within Highly Dynamic River Systems. *Aquatic Sciences*, 71, 279–289.

Turitto, O., Audisio, C. & Agangi, A. (2008) Ruolo svolto da piene straordinarie nel rimodellare la geometria di un alveo fluviale. *Alpine and Mediterranean Quaternary*, 21(1B), 303–316.

Turitto, O., Baldo, M., Audisio, C. & Lollino, G. (2010) A LiDAR application to assess long-term bed-level changes in a cobble-bed river: the case of the Orco River (North-Western Italy). *Geografia Fisica e Dinamica Quaternaria*, 33(1), 61–76.

Vanmaercke, M., Poesen, J., Govers, G. & Verstraeten, G. (2015) Quantifying human impacts on catchment sediment yield: a continental approach. *Global and Planetary Change*, 130, 22–36.

Vautier, F., Corenblit, D., Hortobgyi, B., Fafournoux, L. & Steiger, J. (2016) Monitoring and reconstructing past biogeomorphic succession within fluvial corridors using stereophotogrammetry. *Earth Surface Processes and Landforms*, 41(10), 1448–1463.

Vesipa, R., Camporeale, C. & Ridolfi, L. (2015) Noise-driven cooperative dynamics between vegetation and topography in riparian zones. *Geophysical Research Letter*, 42(19), 8021–8030.

Viles, H. (2020) Biogeomorphology: past, present and future. *Geomorphology*, 366, 106809.

Walcker, R., Corenblit, D., Julien, F., Martinez, J.-M. & Steiger, J. (2021) Contribution of meandering rivers to natural carbon fluxes: evidence from the Ucayali River, Peruvian Amazonia. *Science of the Total Environment*, 776, 146056.

Wheaton, J.M., Brasington, J., Darby, S.E. & Sear, D.A. (2010) Accounting for uncertainty in DEMs from repeat topographic surveys: improved sediment budgets. *Earth Surface Processes and Landforms: The Journal of the British Geomorphological Research Group*, 35(2), 136–156.

Williams, R. (2012) DEMs of difference. In: Clarke, L., Nield, J.M. (Eds.) *Geomorphological techniques*. London: British Society for Geomorphology.

Wohl, E. (2018) *Sustaining river ecosystems and water resources*. Cham: Springer.

Wolman, M.G. (1954) A method of sampling coarse river-bed material. *Transactions of the American Geophysical Union*, 35, 951–956.

Zhu, R., Tsubaki, R. & Toda, Y. (2023) Effects of vegetation distribution along river transects on the morphology of a gravel bed braided river. *Acta Geophysica*, 2023, 1–16.

SUPPORTING INFORMATION

Additional supporting information can be found online in the Supporting Information section at the end of this article.